THE ATOMIC-SCALE STRUCTURE OF DILUTE TIN IN ALUMINUM

by

Peter R. G. Small

A thesis submitted to the Faculty and the Board of Trustees of the Colorado School of Mines in partial fulfillment of the requirements for the degree of Master of Science (Physics).

Golden, Colorado
Date 24 July 1989

Signed: Peter R. G. Small

Approved: Timothy M. Hayes
Dr. Timothy M. Hayes
Thesis Advisor

Don L. Williamson
Dr. Don L. Williamson
Thesis Advisor

Golden, Colorado
Date 24 July 1989

F. D. Schowengerdt 7/24
Dr. Franklin D. Schowengerdt
Professor and Head
Physics Department

ABSTRACT

Fluorescence-detection extended x-ray absorption fine structure (EXAFS) spectroscopy measurements were made on two dilute AlSn alloys, 10 ppm Sn and 50 ppm Sn, and on Sn-ion-implanted Al (dose 5×10^{17} ions/cm^2). This is the first EXAFS investigation of such dilute alloys (<100 ppm) and one of the first examining an ion-implanted material. The data were fit with curved-wave calculated scattering parameters and an experimental β-Sn spectrum. The Sn-Al nearest neighbor (nn) distance was determined to be (2.98 ± 0.03)Å, an increase of ~ 0.12 Å over the Al nn distance, 2.86 Å. This result is equal to the sum of the metallic radii of Al and Sn. The Sn in these samples is not, however, completely in solid solution. Evidence is found for Sn clustering even for these dilute amounts. The results obtained for the 10 and 50 ppm samples are consistent with previous research on grain boundary segregation of Sn in Al. The ion-implanted sample shows no evidence for Sn in solution. The structure of this material is found to be similar to β-Sn possibly modified by defects introduced into the material by the ion-implantation process.

For measuring the small fluorescence x-ray signal, a parallel-plate gas ionization detector with amplifying current-to-voltage converter was built. Problems were identified after its initial use which were subsequently understood and then corrected. These included microphonic noise, capacitive decay, and DC offset. It was also found that covering

the exposed walls of the detector with Pb reduced the background signal by a factor of ten. The changes that were made increased the signal-to-noise ratio of the measured fluorescence signal considerably.

TABLE OF CONTENTS

LIST OF FIGURES

Page

LIST OF TABLES

ACKNOWLEDGEMENTS

I wish to thank my wife, Susanne Small, and my daughter, Stephanie Small, for their patience and support without which I would not have completed this thesis.

I also wish to thank my advisors, Timothy Hayes and Don Williamson, for their help and support, the members of my thesis committee, Thomas Furtak and Noboru Wada, the Amorphous Materials Center for funding a major part of the research, F. G. Bridges for providing the plans for the sample holder/dewar, P. Lagarde for providing experimental aluminum spectra, and Lap Nguyen for annealing the AlSn samples.

Chapter 1

INTRODUCTION

The binary alloy system of tin in aluminum is very interesting from a metallurgical point of view. Tin (Sn) and aluminum (Al) are two essentially immiscible metals. Due to the large atomic volume of Sn atoms, it is very difficult for them to fit into the Al lattice. The metallic radius (radius of atom in 12-coordinated metals) is 1.43 Å for Al and 1.55 Å for Sn [1]. In addition, Al occurs in the face-centered cubic structure, while β-Sn (white Sn), the stable phase at room temperature, is found in a more complicated tetragonal lattice with a four atom basis, shown in Figure 1.1 [2]. The differences between these two metals, which is reflected in their effective sizes and crystal structures, is the reason for their unusual behavior in an alloy. The equilibrium solid solubility of Sn in Al has been found to be very low, reaching a maximum of approximately 0.10 weight percent (wt. %) (0.02 atomic percent [at. %]) at 900 K (Figure 1.2) [3]. As much as 1.2 wt. % (0.23 at. %) Sn can be held in solution by quenching from the liquid [4] and a solid solubility of 6 wt. % (1.2 at. %) Sn can be obtained by vapor deposition [4]. In the dilute Sn in Al alloys studied (hereinafter referred to as <u>Al</u>Sn), the exact Sn environment in the host lattice is not known. The Sn atoms may be dispersed in a solid solution or clustered at grain boundaries or within the grains themselves.

The <u>Al</u>Sn alloy system is of interest because Sn is used in dilute

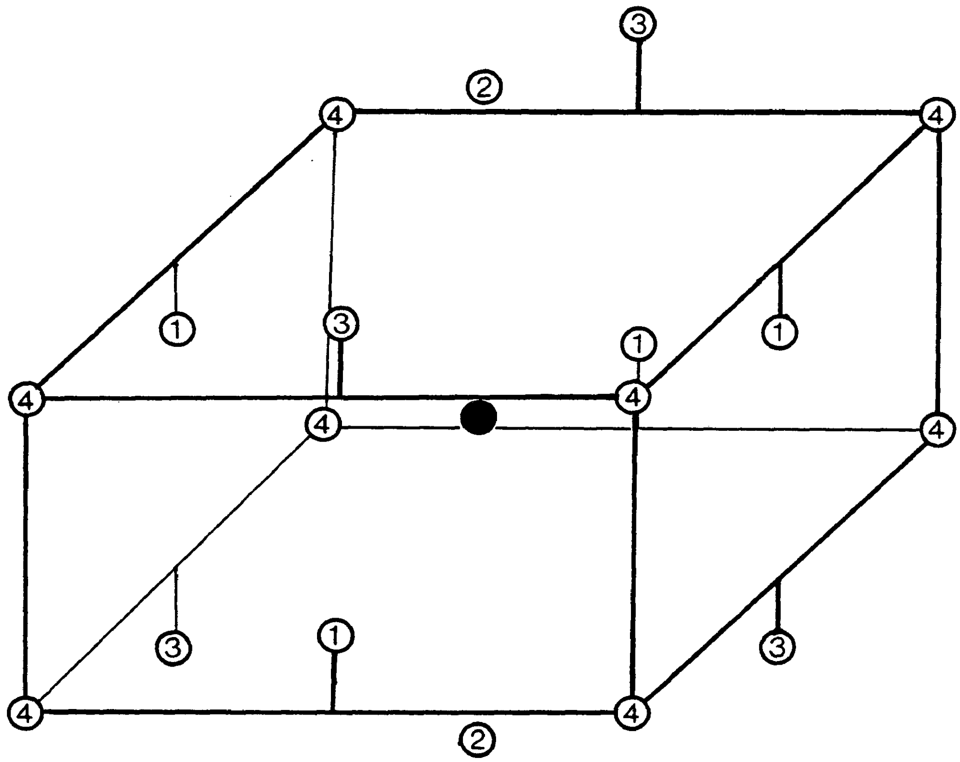

Figure 1.1 Crystal Structure of β-Sn.
The neighbor shells are indicated by their number.

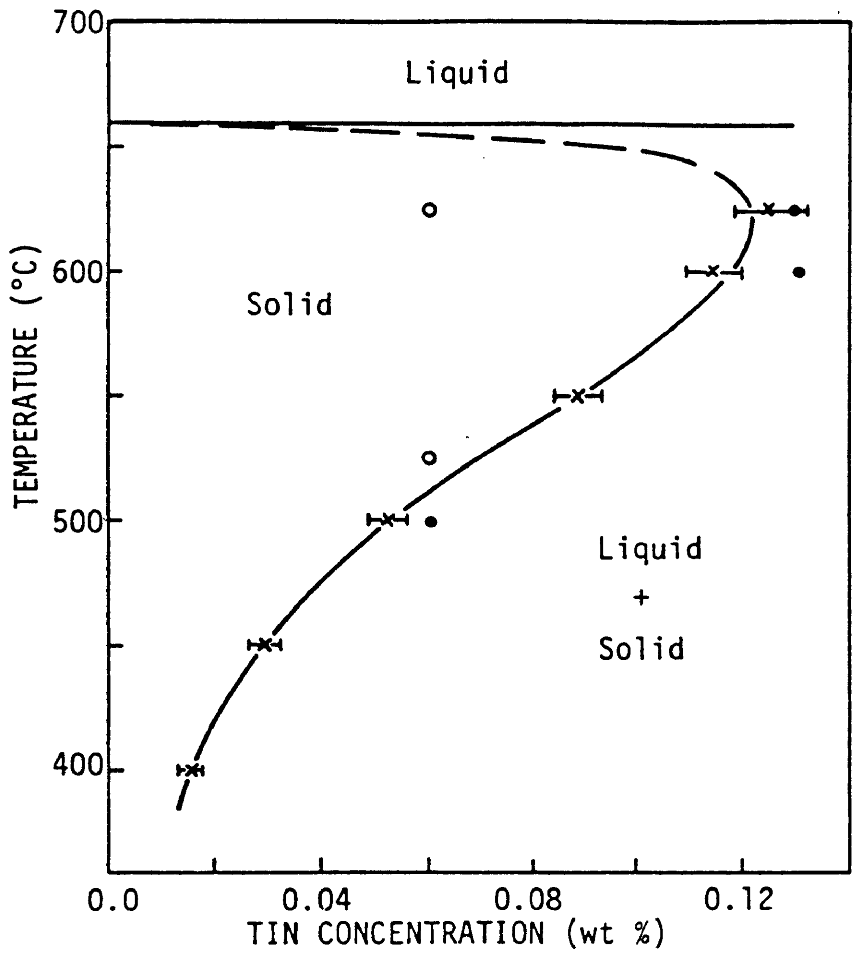

Figure 1.2 Solid Solubility of Sn in Al versus temperature [3].

amounts with Al in the manufacture of bearings and has been found to modify dramatically the age-hardening behavior of Al-copper alloys [3]. In 1968, Aust et al. [5] described hardness experiments performed on the dilute alloy systems of PbCa, PbU, SnPb, SnSb, ZnAl, and ZnAu. They measured the hardness profile over grain boundaries using a Kentron microhardness tester with a pyramidal diamond indentor. The hardness was measured at various points along lines perpendicular to grain boundaries. In all cases of pure elements, the grain boundaries were softer than the grains themselves. The addition of certain alloying elements in low atomic concentrations caused hardening at the grain boundaries.

This excess hardening was proposed to be caused by solute atoms migrating to the grain boundaries and clustering there according to the following model. As the alloys are cooled (or quenched) from the melt, vacancies are frozen in solid solution. Because of this, the number of vacancies at room temperature is greater than the thermodynamic equilibrium value. This leads to a tendency for vacancies to migrate to grain boundaries or free surfaces where relaxation can occur. Solute atoms with a positive vacancy binding energy would, therefore, be drawn along with the vacancies towards these boundaries. Collisions between vacancy-solute atom pairs will form clusters of solute atoms, the highest concentration of these being right at the grain boundaries. It was found that solute atoms which increase the grain boundary hardness all have a positive vacancy binding energy.

Using this theoretical model as a basis, microhardness measurements were made by Eadie and Aust [6] on the AlSn system for Sn concentrations of 10 and 50 atomic parts per million (at. ppm). Sn in Al has a large positive vacancy binding energy, which the model predicts will cause grain boundary hardening. It was found that the hardness at the grain boundaries increased by 2 to 4 % over that for pure Al. Independent investigation by Westbrook and Peat [7] determined grain boundary hardening in excess of 9 %.

Other experiments on the AlSn system were performed by Erb and Aust [8]. In these experiments, TEM (transmission electron microscopy) micrographs of grain boundaries were taken and the dispersion of Sn measured using the x-ray microprobe of the TEM. The x-ray microprobe detects and energy-resolves the fluorescent x-rays emitted by atoms excited by the electrons of the TEM and is able to determine the types of atoms present in a small area (9 nm in diameter in this experiment) by their characteristic fluorescent x-ray energies. After annealing for several hours at various temperatures, they detected Sn-rich inclusions forming near grain boundaries. Also carried out by these authors [9] was an investigation of the corrosion behavior of AlSn(280 ppm). It was observed that the grain boundaries corrode faster than the surrounding grains.

Most recently, strain amplitude measurements at grain boundaries of AlSn(11 ppm) were carried out by Iwasaki [10]. It was again determined that there is excessive Sn clustering at grain boundaries at a concentration of around 440 ppm. In addition, synchrotron radiation microradiology studies of <u>Al</u>Sn indicate that, as the alloy is cooled, pure Al grains form separated by a layer of <u>Al</u>Sn [11].

Mössbauer effect measurements have also been made on the <u>Al</u>Sn system [12 to 16]. A single broad Mössbauer feature was resolved and interpreted in terms of three constituent lines, and the electron density and electric field gradient at the Sn nuclei were calculated. These Sn sites in Al were associated with vacancies (three different sites with 2, 3, and 4 vacancies), Sn in solution and Sn clustering, with a certain percentage of Sn in each site depending on the sample preparation. The exact structure, however, in terms of neighbor distance, type and number can not be measured directly using this technique.

A direct determination of the Sn environment in Al is needed to enable better interpretation of other experiments on dilute alloys, such as the Mössbauer effect, provide confirmation or rejection of lattice defect models, and also assist in developing theories of impurity segregation in metals. This need was addressed in this thesis research using extended x-ray absorption fine structure (EXAFS) spectroscopy. Results have been obtained for three <u>Al</u>Sn alloys: 50 ppm and 10 ppm Sn and Al ion-implanted with Sn (dose 5×10^{17}). In addition, this determination provides an <u>Al</u>Sn EXAFS signature which can be used in the EXAFS analysis of other interesting materials, such as $Ga_xAl_{1-x}As$:Sn.

Chapter 2
TECHNIQUE OF EXAFS

Theory of EXAFS

An x-ray photon can interact with an atom in two ways: it can be scattered by the electrons of the atom (Compton scattering) and it can be absorbed by the atom with the ejection of an electron (photoelectric effect). The extended x-ray absorption fine structure (EXAFS) has its origins in the photoelectric effect with absorption of x rays by atoms in a molecule or solid. When an atom in a solid absorbs an x ray with sufficiently high energy E_x, an innermost shell electron can be excited out of the atom core and into an unoccupied state (i. e., above the Fermi energy of the solid) with an energy $E_x - E_K$, where E_K is the binding energy of the K-shell electrons of the atom. The electron then leaves the atom as a spherical wave. As it propagates outward, it is reflected from neighboring atoms with a smaller probability. These reflected electron waves interfere with the initial out-going wave at the excited atom, causing a modulation in the absorption coefficient of the atomic species.

Shown in Figure 2.1 is the K-shell x-ray absorption spectrum of β-Sn. The x-ray absorptance, the product of the x-ray absorption coefficient $\mu(E_x)$ and the sample thickness, is plotted versus x-ray energy, E_x. The large increase in the absorptance corresponds to the threshold for the excitation of a K-shell electron to the continuum

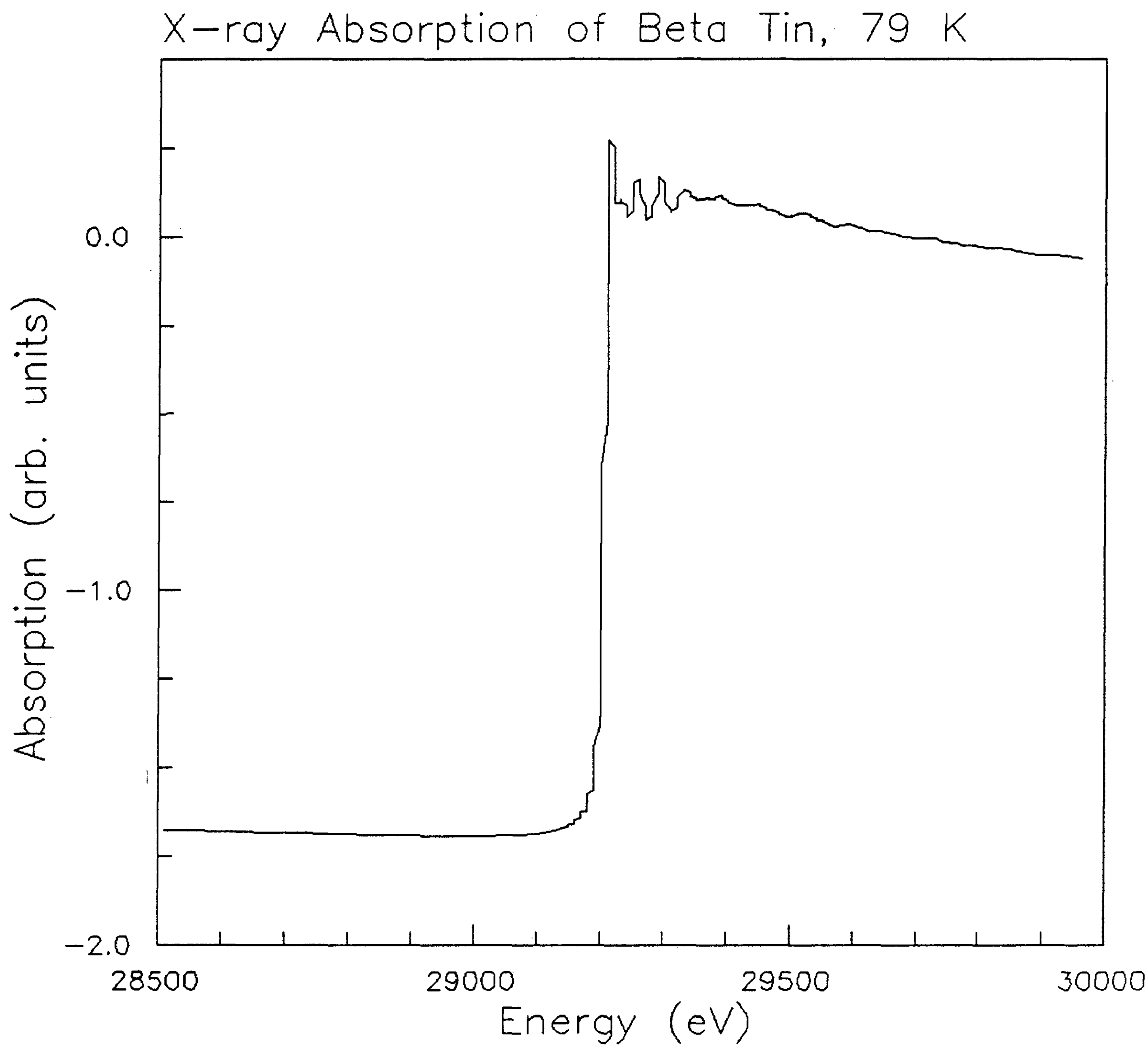

Figure 2.1 X-Ray Absorption Spectrum of β-Sn.

(called the K-shell absorption edge). The EXAFS is the oscillations of the x-ray absorption coefficient above the absorption edge. This modulation is due to the phase shift between the initial outgoing wave and the reflected wave. The principal contribution to the phase shift is equal to 2kr, where k is the wave vector of the electron wave and r is the distance between the emitting atom and the backscattering atom. k is related to the x-ray energy and the absorption edge energy by the relation,

$$k \simeq \frac{\sqrt{2m}}{\hbar} (E_x - E_K)^{\frac{1}{2}}. \qquad (2.1)$$

In addition, the potentials of the excited atom and the backscattering atoms contribute energy-dependent terms to the phase shift. The amplitude of the backscattered wave is governed by the potential of the backscattering atom, the attenuation of the wave in traversing the distance 2r, and thermal broadening.

It has been experimentally verified that, unlike low energy electron diffraction (LEED) which can be treated theoretically only by multiple scattering theory, the EXAFS can be adequately explained by single scattering theory (as long as the data analyzed does not include that in the neighborhood of the absorption edge). This simplifies calculations and data analysis considerably. The following equations show explicitly the contributions of the above mentioned effects to the EXAFS [17]. The total x-ray absorption coefficient for excitation of a K-shell electron from an atom of type a is given by:

$$\mu_s(E_x) = \mu_{bg}(E_x) + \mu_a(E_x), \qquad (2.2)$$

where

$$\mu_a(E_x) = \mu^o{}_a(E_x)[1 + \chi_a(E_x)]. \tag{2.3}$$

$\mu_{bg}(E_x)$ is the background absorption by other atomic species and by other shells of the same atomic species; it is a continuous function of energy. $\mu^o{}_a(E_x)$ is similar to the absorption coefficient for free atoms and contains the absorption edge (but otherwise is essentially featureless). The oscillatory behavior (i.e., the EXAFS) is contained in $\chi_a(E_x)$. This has been extracted from the x-ray absorption spectrum of Figure 2.1 using the techniques described in Chapter 5 and is shown in Figure 2.2. With these considerations, the EXAFS of atomic species a can be expressed as,

$$k\chi_a(k) = \Sigma_b \int_0^\infty dr\ r^{-2}\ p_{ab}(r)\ 2\mathrm{Re}[e^{i2kr}\ \Lambda_{ab}(k,r)] \tag{2.4}$$

with

$$\Lambda_{ab}(k,r) \simeq (2i\pi^2 m/\hbar^2)t^+{}_b(-\underline{k},\underline{k})\exp[-2r/\lambda(k) + 2i\delta_a(k)] \tag{2.5}$$

From equations (2.4) and (2.5), the various contributions to the EXAFS become apparent. Structural information is contained in $p_{ab}(r)$ and energy dependent scattering information in $\Lambda_{ab}(k,r)$. $p_{ab}(r)$ is the atomic pair correlation function of atomic species b about atom a. This describes the distance distribution between the excited atomic species a and its neighbors of type b. Temperature dependence is contained in this term via the mean-square-relative-displacement between the excited atom and its neighbors, which appears in a factor similar to a Debye-Waller factor. $\Lambda_{ab}(k,r)$ includes the many energy-dependent

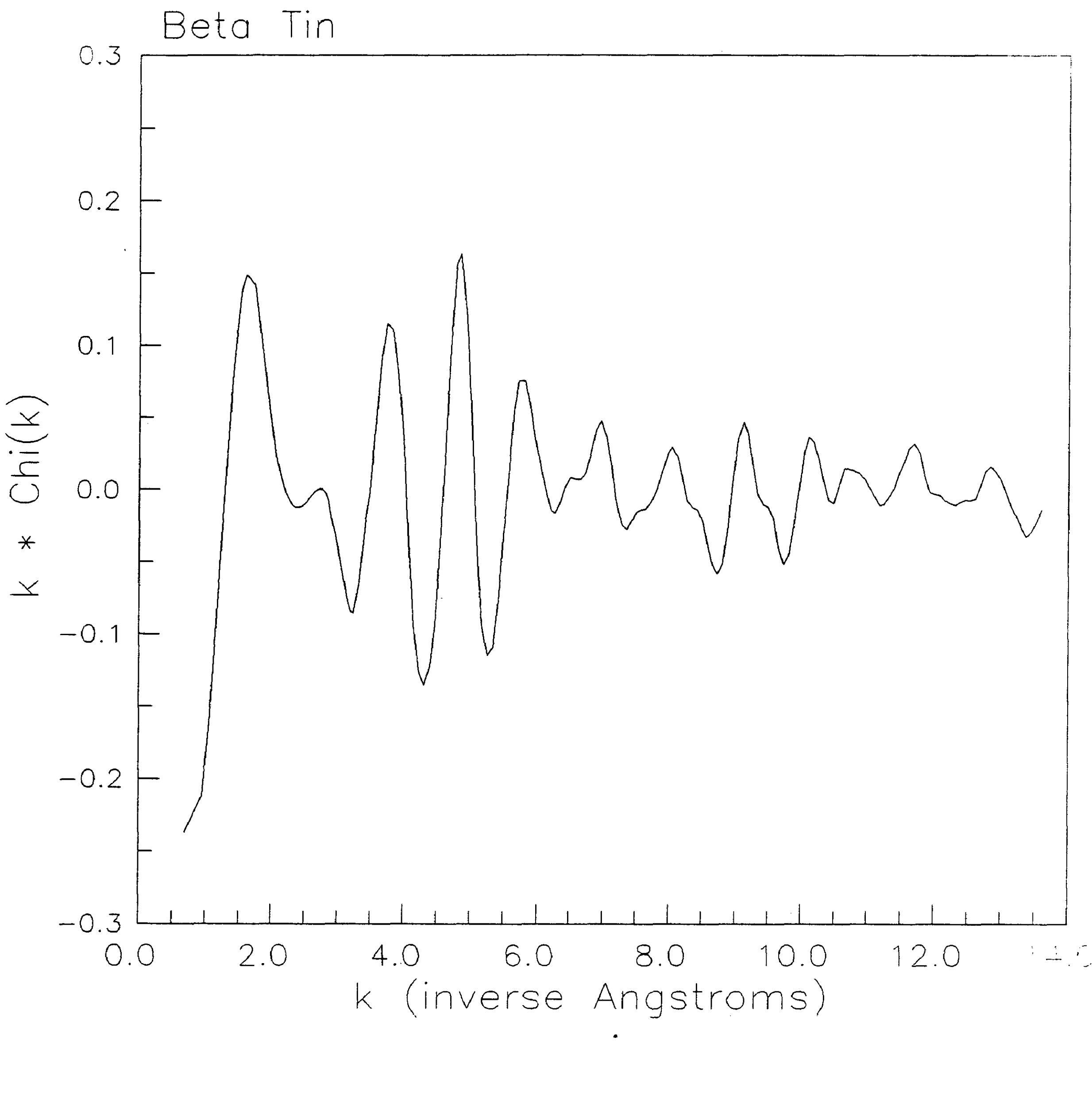

Figure 2.2 $k\chi(k)$ of β-Sn.
Extracted from the data in Figure 2.1.

effects which are a result of the interaction between the emitted electron and the potentials of the excited atom, a, and the backscattering atoms, b. $t^{+}_{b}(-\underline{k},\underline{k})$ is the complex backscattering t-matrix of the scattering atom. $\lambda(k)$ is the electron mean-free-path and δ_a is the l=1 phase shift due to the potential of the excited atom.

In order to analyze the structural information contained in $k\chi_a(k)$, it is often convenient to Fourier transform this quantity. After transforming, the peaks in $p_{ab}(r)$ ideally become separated, simplifying the analysis. With 2k and r as complementary variables, the Fourier transform (FT) of $k\chi(k)$ can be expressed to a good approximation as [17]:

$$\varphi_a(r) \simeq \Sigma_b \int_0^{\infty} dr' \; r'^{-2} \; p_{ab}(r') \; \xi_{ab}(r-r'), \qquad (2.6)$$

for $r > 0$. $\varphi_a(r)$ is the convolution of a pair correlation function, $p_{ab}(r)$, with a peak function, $\xi_{ab}(r-r')$, where $\xi_{ab}(r-r') = \mathrm{FT}[W(k) \times \Lambda_{ab}(k,r)]$. W(k) is a window function introduced to account for the finite extent of the data in k-space. It is discussed further in Chapter 5. The Fourier transform of $k\chi(k)$, $\varphi(r)$, for β-Sn is shown in Figure 2.3. The actual positions of the first through fifth atomic shells are indicated by arrows. The peaks in $\varphi(r)$ are shifted from the peaks in p_{ab} due to the k-dependence of the phase shifts of the excited atom and backscattering atoms.

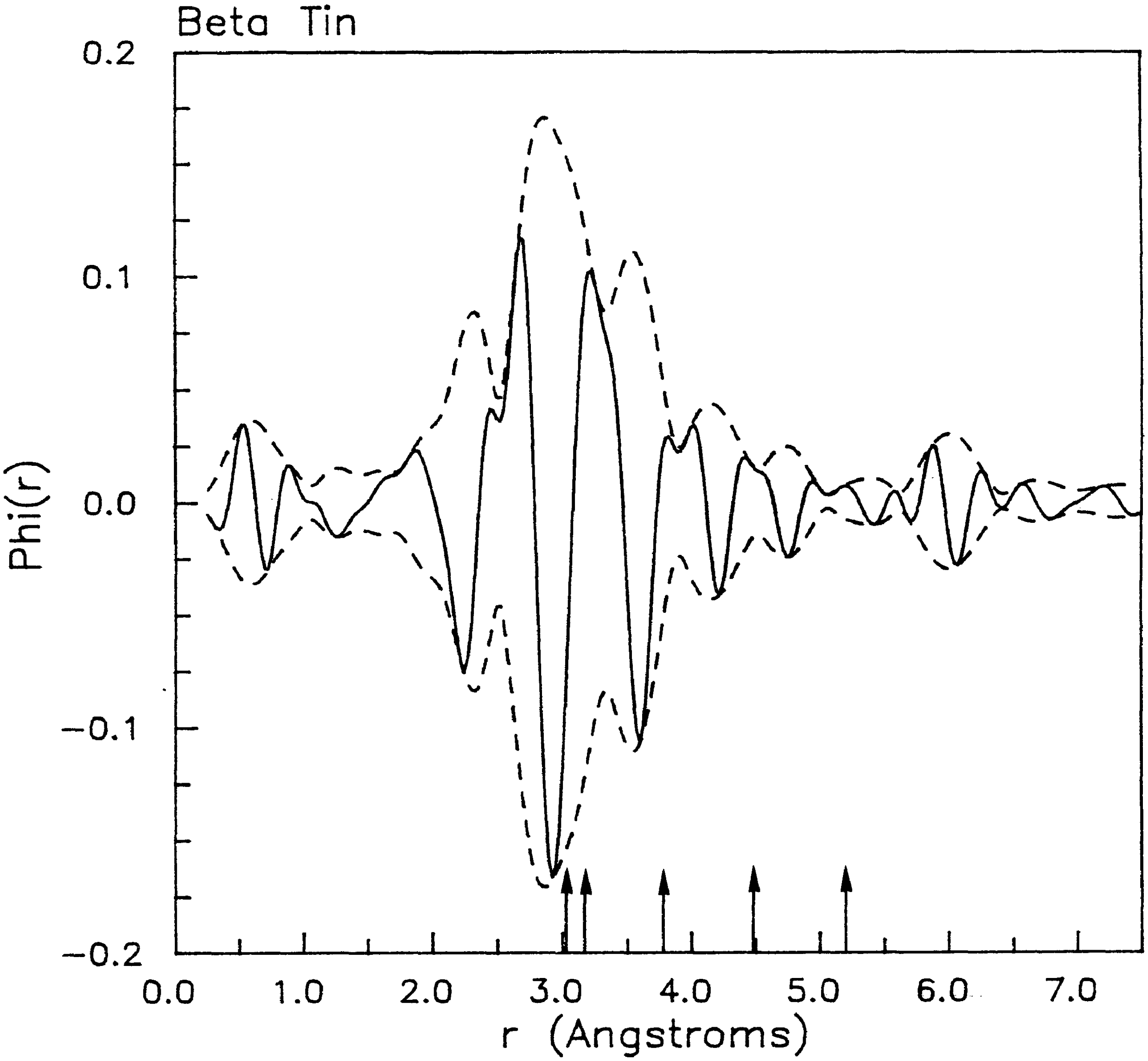

Figure 2.3 $\varphi(r)$ of β-Sn.
Fourier transform of data in Figure 2.2 (limits: 2.20 to 13.67 $Å^{-1}$)
(dashed line = $|\varphi(r)|$, solid line = $Re[\varphi(r)]$)

EXAFS Measurements

To measure the EXAFS of a particular atomic species in a crystal, the energy of an incident x-ray beam is scanned over the x-ray absorption edge of, usually, the K-shell electrons of a particular atomic species. For the measurements made in this project, the Sn K-edge at ~ 29.2 keV was used. The absorption of this beam by the atomic species is measured either by measuring the transmittance of the x-ray beam directly or by measuring the secondary products of absorption. There were two types of EXAFS measurements made on the samples analyzed: transmission and fluorescence-detection.

Transmission EXAFS. In transmission, the x-ray beam passes directly through the sample and is attenuated according to the usual attenuation law,

$$I(E_x,z) = I_0(E_x)\exp[-\mu(E_x)z], \tag{2.7}$$

where $I(E_x)$ is the intensity of the x-ray beam in, e.g., photons per second with energy E_x, z is the sample thickness and $\mu(E_x)$ is the absorption coefficient of the atom of interest which was described above. In EXAFS measurements, z is constant; changing the energy changes $\mu(E_x)$. The experimental arrangement for a transmission experiment is shown in Figure 2.4. The sample is oriented perpendicular to the x-ray beam. The beam intensity is measured before and after passing through the sample. The x-ray absorptance, which is the x-ray absorption coefficient times the sample thickness is then calculated as

$$\mu(E_x)z = \ln\,[I_0(E_x)/I(E_x)], \tag{2.8}$$

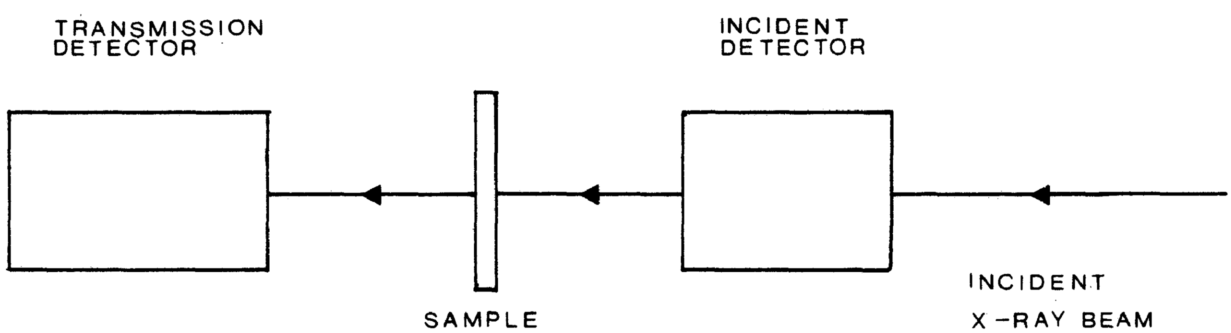

Figure 2.4 Experimental Arrangement for Transmission EXAFS.

and plotted as a function of energy (Figure 2.1). The transmission method works well for samples with large concentrations of absorbing atoms because the modulations in the absorption coefficient are larger than the statistical noise in the transmitted x-ray beam.

Fluorescence-Detection EXAFS. The EXAFS in samples with dilute concentrations of absorbing atoms cannot be measured by the transmission method because the signal-to-noise ratio (S/N) for the transmitted beam would be too small. For example, if the concentration of absorbing atoms is 10^{-4} (100 ppm), then an absorption edge ~ 10^{-4} above the background and modulations << 10^{-5} would have to be detected. An incident x-ray beam with an intensity of 10^{10} photons per second has statistical noise with intensity of ~ 10^{-5} of the incident beam for a typical value of the integrating time (~ 1 sec). Therefore, the modulation of the x-ray absorption coefficient would be lost in the statistical noise of the beam. In addition, in real experiments there is usually noise in the incident x-ray beam which is larger than the statistical noise, arising from fluctuations in the beam position. The concentration limit considering only statistical noise for making transmission EXAFS measurements has been determined to be ~ 0.5 % [17]. In order to measure the EXAFS due to dilute species one must use other methods which are not dependent upon the statistics of the transmitted beam. Fluorescence- and Auger-electron-detection EXAFS are two such techniques.

After an atom absorbs an x ray, the atom is left in an excited state. In order to return to a state of equilibrium, the atom must release this excess energy by the emission of either fluorescent x rays or Auger electrons. Fluorescence- and Auger-electron-detection EXAFS are based upon measuring the flux of these secondary emissions. Atoms with atomic number greater than 30 (zinc) have a greater probability of x-ray emission when a K-shell electron is excited. Sn has an atomic number of 50 and therefore fluorescence-detection EXAFS was used to measure the absorption.

As the energy of the x-ray beam, E_x, changes, the energy of the fluorescent x rays, E_f, dependent upon the atom species and the electronic shells involved, remains constant. Detection schemes have been devised to detect these x rays preferentially. The experimental arrangement for fluorescence-detection EXAFS is shown in Figure 2.5. The intensity of the x-ray beam is measured before passing through the sample. The sample is oriented at an angle of 45° with respect to the incident x-ray beam and the fluorescent x-ray detector placed at 90° to the beam for reasons described in Chapter 4. For a sample of thickness z, with absorbing atomic species a, emitting fluorescent x rays with energy E_f, the intensity of the emitted fluorescent x rays is [17]:

$$I_f(E_f) = I_0(E_x)\epsilon_f(\Omega/4\pi)\{\mu_a(E_x)/[\mu_s(E_x) + \mu_s(E_f)]\}$$
$$\times(1 - \exp\{-[\mu_s(E_x) + \mu_s(E_f)]z/\surd 2\}). \qquad (2.9)$$

Ω is the solid angle subtended by the detector as seen from the sample. $\mu_s(E_x)$ and $\mu_a(E_x)$ are defined in equations (2.2) and (2.3). ϵ_f is the fluorescent yield, the probability that the atom will undergo a

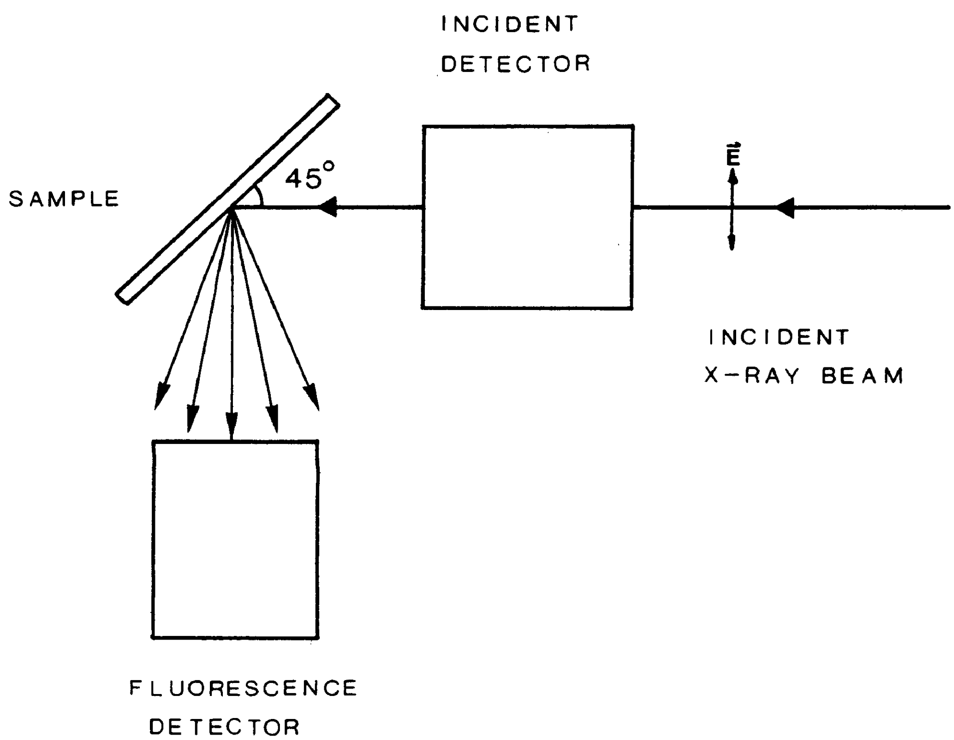

Figure 2.5 Experimental Arrangement for Fluorescence-Detection EXAFS. (Top View).

radiative decay (versus an electronic decay). For thick samples, this reduces to [17]:

$$I_f(E_f) = I_0(E_x)\ \epsilon_f\ (\Omega/4\pi)\ \{\mu_a(E_x)/[\mu_s(E_x) + \mu_s(E_f)]\} \tag{2.10}$$

In fluorescence experiments, $I_0(E_x)$ and $I_f(E_f)$ are measured. Their ratio, $I_f(E_f)/I_0(E_x)$, gives an absorption spectrum like that shown in Figure 2.1, which resembles that of transmission EXAFS. For any EXAFS to be detected, μ_a must not be the dominant contribution to μ_s. If $\mu_s \approx \mu_a$, the quantity in curly braces in equation (2.10) is constant with respect to E_x, containing no EXAFS. A small μ_a yields a small I_f, but one in which EXAFS is present.

Signal-to-Noise

If the S/N for the transmission and fluorescence-detection EXAFS are compared, the strengths of each become apparent. In making EXAFS measurements, χ_a is the signal and the noise investigated is only the statistical noise of the incident x-ray beam. The following equations were derived in Reference 17. For transmission with optimized sample thickness,

$$S/N = 0.736\ N_0^{1/2}\ \chi_a(k)\ (\mu_a^{o}/\mu_s), \tag{2.11}$$

and for fluorescence-detection,

$$S/N = \chi_a(k)\ (\epsilon_f\Omega/4\pi)^{1/2}\ N_0(E_x)^{1/2}\{\mu_a^{o}/[\mu_s(E_x)+\mu_s(E_f)]\}^{1/2} \times\{[\mu_{bg}+\mu_s(E_f)]/[\mu_s(E_x)+\mu_s(E_f)]\}[1+I_{bg}/I_f]^{-1/2}. \tag{2.12}$$

N_0 is I_0 times the integrating time. Looking at equations (2.11) and (2.12), we see that the S/N for fluorescence-detection EXAFS is approximately proportional to $[\mu_a^{o}(E_x)/\mu_s(E_x)]^{1/2}$, while that for transmission is proportional to $[\mu_a^o(E_x)/\mu_s(E_x)]$. For dilute samples, $\mu_a(E_x)$ is much smaller than $\mu_s(E_x)$, their ratio being on the order of 10^{-4} to 10^{-6}. This factor, therefore, is several orders of magnitude larger in fluorescence-detection than in transmission. Thus, fluorescence-detection EXAFS is better suited for making measurements on dilute atomic species.

In EXAFS spectra, we want the amplitude of the EXAFS oscillations at the end of the spectrum to be at least as large as the noise, i.e. S/N ~ 1. At k = 12 $Å^{-1}$, which is near the end of the spectra measured, $\chi_a(k) \sim 0.003$. For concentrated samples, $\mu_a/\mu_s \sim 1$ and a transmission spectrum will require $N_0 \sim 10^6$ photons per point to achieve S/N ~ 1 at this value of k. For dilute samples, $\mu_a/\mu_s \sim 10^{-4}$. A transmission spectrum will require $N_0 \sim 10^{14}$ and a fluorescence-detection spectrum will require $N_0 \sim 10^{12}$. At this value of k, the integrating time is ~ 10 s. Thus, to achieve large enough S/N for adequate structural determination using fluorescence detection, $I_0 \sim 10^{11}$ photons/sec. If I_0 is smaller than this value, the S/N can be improved by adding together several spectra (see Chapter 5).

This condition makes EXAFS very impractical using most conventional bremsstrahlung x-ray sources because the intensity of this radiation is not very great, ~10^3 to 10^4 photons/sec. The intense x radiation generated by synchrotrons and electron storage rings (called synchrotron radiation) is better suited for making EXAFS measurements, having a photon flux >10^8 photons/sec. To get a comparable number of counts, an x-ray absorption spectrum made with a bremsstrahlung source will take several days, while the same made using synchrotron radiation will take several minutes. Figure 2.6 [18] shows a comparison between the spectral and intensity characteristics of synchrotron radiation sources and conventional bremsstrahlung sources. At the Sn K-edge, 29.2 keV, synchrotron radiation is at least 10^4 times as bright as bremsstrahlung radiation, which gives an increase in S/N of ~ 100 for identical counting times. The wiggler beam lines which were used to measure the data in this thesis produced intensities > 10^{10} phonons/sec at the Sn K-edge.

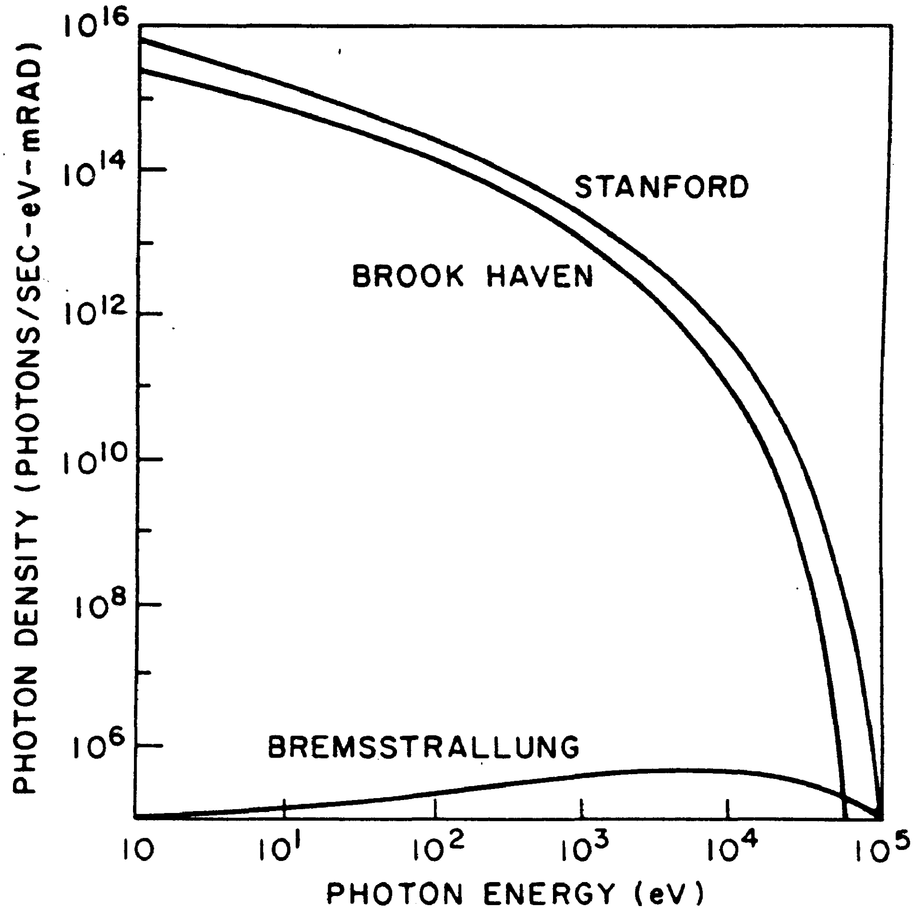

Figure 2.6 Comparison of Synchrotron Radiation with Bremsstrahlung Radiation [18].

Chapter 3

EXPERIMENTS

The EXAFS experiments were performed at the Stanford Synchrotron Radiation Laboratory (SSRL) in Palo Alto, California. SSRL uses an electron storage ring, SPEAR (Stanford Positron Electron Accelerating Ring), as a source of high intensity synchrotron x radiation. Experiments were conducted in an enclosure called a hutch, which shielded the experimenters from the x-ray beam. The experimental arrangement is shown in Figure 3.1. There are four basic parts to this apparatus: the silicon crystal monochromator, the sample table, the sample holder/dewar, and the x-ray detectors. The major parts of the experiment are computer controlled by a PDP-11 computer with the RSX-11 operating system.

Experimental Apparatus

Silicon Crystal Monochromator. A silicon crystal monochromator is used to make the incident synchrotron radiation monochromatic in energy. It consists of two parallel silicon crystals cut parallel to a certain Bragg plane (Figure 3.2) [18]. Two crystals are used so that after diffracting from both crystals, the monochromatic beam is parallel to the incident beam. Through the Bragg condition the white synchrotron radiation is made essentially monochromatic. The Bragg condition is

$$n\lambda = 2d \sin\theta, \tag{3.1}$$

where λ is the wavelength of the x ray, d is the spacing between Bragg

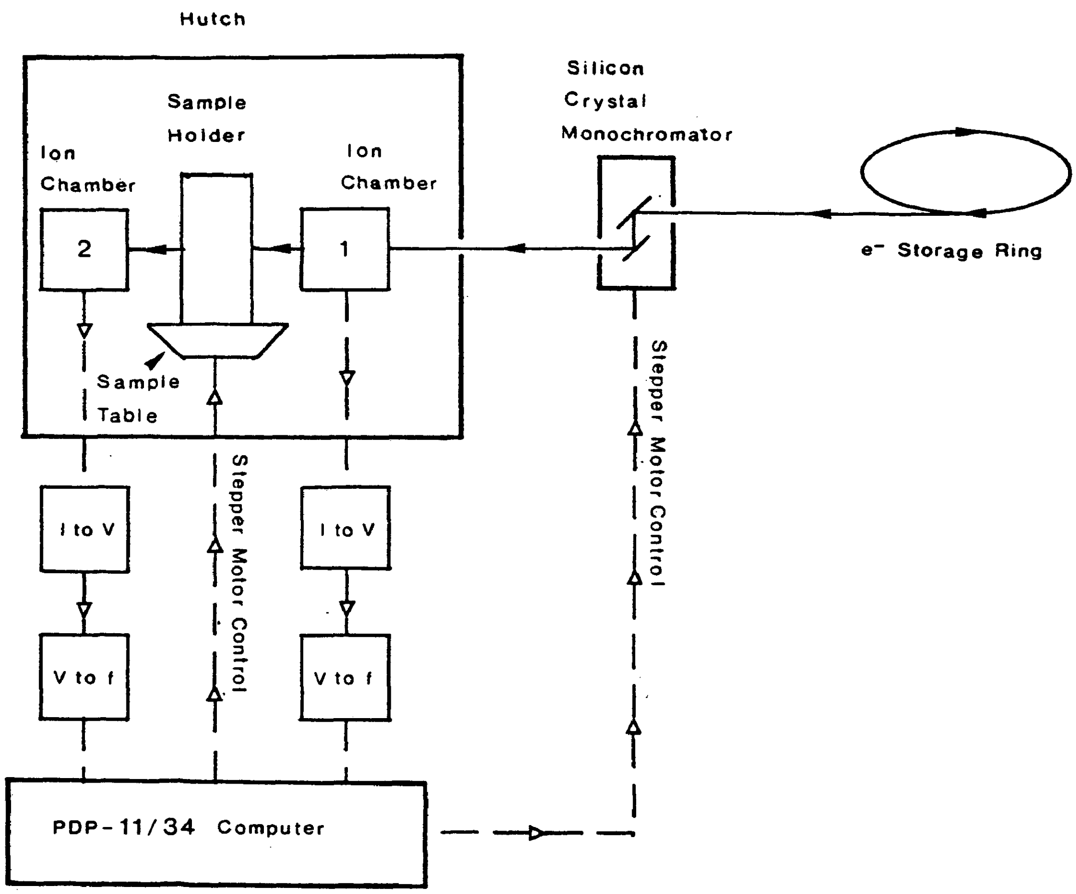

Figure 3.1 Schematic of Experimental Arrangement at SSRL.

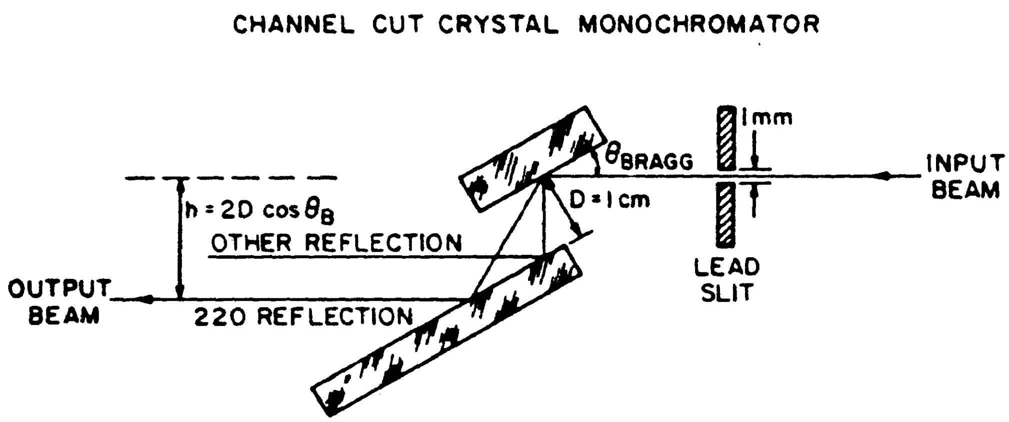

Figure 3.2 Crystal Monochromator [18].

planes, and θ is the angle between the wave vector of the x ray and the Bragg plane (called the Bragg angle). Those x rays with wavelength satisfying the Bragg condition on both crystals will emerge parallel to the incident beam and will be able to enter the hutch through the entrance slit. This results in a nearly monochromatic x-ray beam incident upon the EXAFS sample with central wavelength

$$\lambda = 2d \sin\theta, \tag{3.2}$$

and resolution

$$\Delta\lambda/\lambda = \cot\theta \; \delta\theta_r, \tag{3.3}$$

where $\delta\theta_r$ is the inherent collimation of the incident synchrotron radiation [18]. After diffracting from both crystals, this beam is displaced vertically from the input beam by a distance,

$$h = 2D \cos\theta, \tag{3.4}$$

where D is the separation between the two crystals, usually 1 cm. To change the energy of the x-ray beam entering the hutch, the monochromator crystals are rotated by means of a stepper motor about an axis perpendicular to the beam, changing the Bragg angle and therefore the wavelength of the diffracted x rays. For the experiments described here, the (400) plane of Si was used in the monochromator in order to comply with the angular limitations of the monochromator and to give greater energy resolution at the Sn K-edge (~ 29.2 keV).

After diffracting from the crystals, however, the beam usually contains other x-ray wavelengths which are not centered about the previously described central wavelength. Higher orders (n greater than l in the Bragg condition) of the primary x-ray wavelengths are also diffracted, provided that their geometrical structure factor is not equal to zero. These are called higher harmonics. For a primary beam reflected from the (400) plane of Si (called the [400] beam), the (800) beam is a possible higher harmonic. Higher harmonics cause problems in the normalization of $\chi(k)$. This is discussed further in Section 8 of Reference 17. In addition they increase the background signal, thereby increasing the statistical noise in the beam.

The intensity of the higher harmonics is minimized through a piezoelectric crystal control system which detunes the two crystals, bringing them slightly out of parallel alignment. This changes the Bragg angle of incidence on the second crystal which has a greater effect upon the higher harmonics and prevents these x-rays from striking the sample. This is due to the narrower Darwin width of the higher harmonics. The Darwin width is dependent upon the (hkl) Bragg plane of the monochromator crystal as $(h^2 + k^2 + l^2)^{-1}$. The (800) beam is one fourth as wide as the (400) beam. The angle of incidence on the second crystal can be adjusted so that the diffraction distribution curve of the primary beam at the second crystal overlaps partially with that of the first crystal, while that of the higher harmonics does not. This effectively screens the higher harmonics from striking the sample.

<u>Sample Table</u>. At the entrance to the hutch is a lead entrance slit or collimator which controls the cross sectional area of the beam. This was adjusted to fit the sample dimensions. As the Bragg condition is

satisfied for the various energies of the spectra, the vertical position of the beam at the sample changes as $\cos\theta$. To keep the sample properly aligned, the sample holder is mounted on a movable platform, called the sample table. The sample table tracks the beam as its position changes with energy by means of a stepper motor. Thus the beam is always incident upon the same point on the sample. The intensity of the x-ray beam is not constant with energy, however. It decreases with increasing energy because of the spectral characteristics of the electron storage ring and the intensity dependence of diffraction from the monochromator. The spectral intensity distribution for the beam lines at the Stanford electron storage ring is shown in Figure 2.6.

<u>Sample Holder/Dewar</u>. For these experiments, the samples were placed in a low temperature sample holder/dewar built at CSM (Figure 3.3) based on a design by F. G. Bridges [19]. This apparatus is constructed out of stainless steel and aluminum and consists of a sample chamber partially surrounded by a liquid nitrogen reservoir. The sample chamber is a hollow cylinder 4 cm in diameter and 40 cm in length which is filled with dry helium (He) gas to provide thermal contact with the liquid nitrogen reservoir. The liquid nitrogen reservoir consists of an evacuated chamber 8 cm in diameter and 34 cm in length capped with a styrofoam plug which helps to insulate the liquid nitrogen from room temperature and prevent excessive ice build-up above the liquid nitrogen. To reduce radiative heat transfer, aluminized mylar (25 μm thick) was wrapped about the reservoir inside the evacuated chamber. A

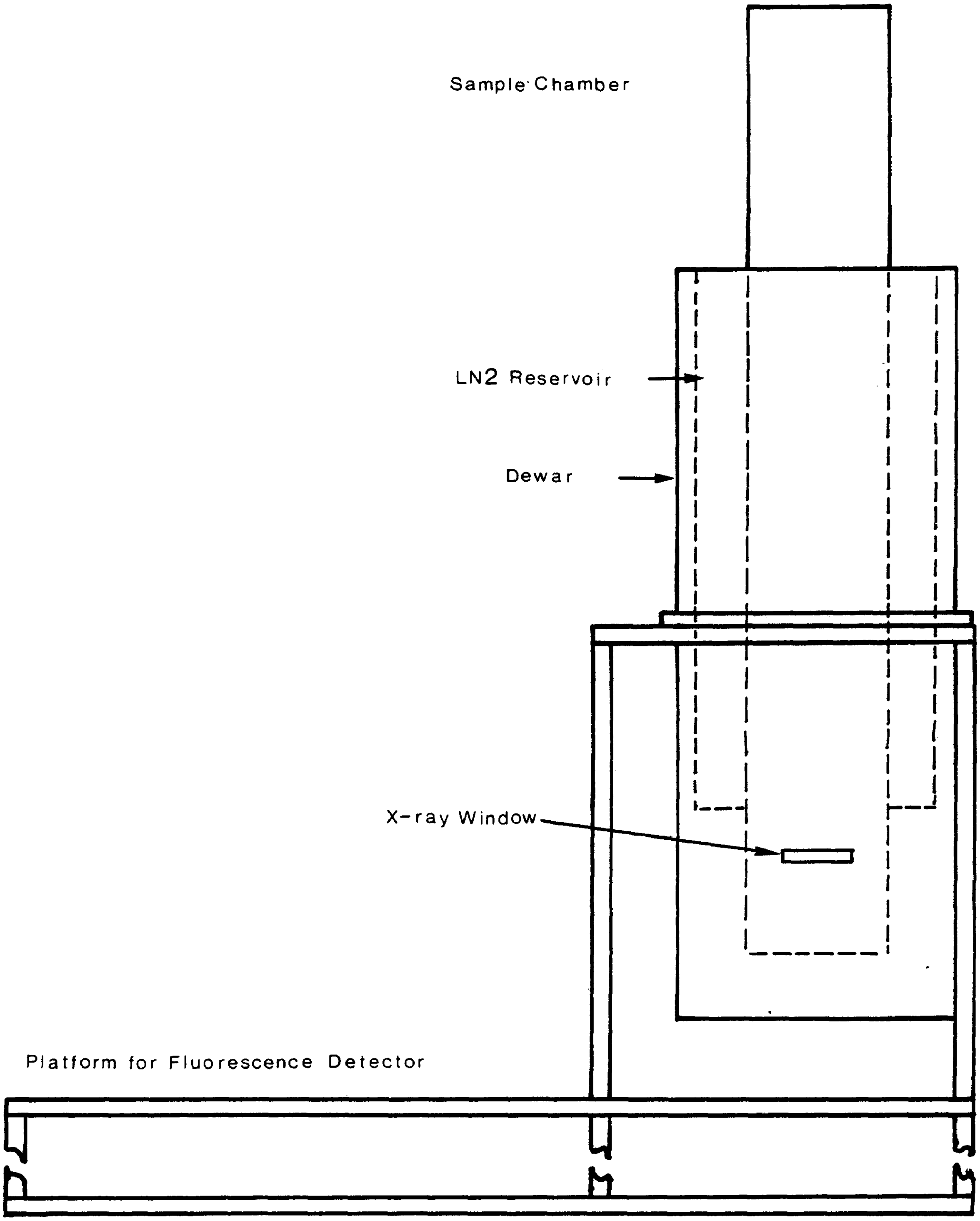

Figure 3.3 Sample Holder/Dewar.

window of Kapton plastic allows the x-ray beam to reach the samples with minimum absorption. The metal supporting the window is aluminum, which was chosen because it has low fluorescence at high values of the incident x-ray energy. The sample holder/dewar is supported by a frame which also contains a platform upon which the x-ray fluorescence detector is placed.

Samples were kept near the temperature of liquid nitrogen (77 K) to reduce the thermal broadening of the EXAFS. While samples were being changed, He was flowed through the sample chamber to prevent water vapor from entering and condensing on the surfaces of the sample chamber and on the samples themselves. Seven samples at a time can be loaded into the holder. They are held onto a slotted rectangle at the end of a rod with vacuum grease (Figure 3.4). To move a sample into the position to be measured, the rod is raised or lowered by inserting or removing spacers which insure that the samples are at the correct height [19].

X-ray Detectors. The x-ray detectors used in measuring the intensities of the three beams (incident, transmitted, and fluorescent) were gas ionization detectors. They produce a current which is proportional to the number of x-ray photons entering the detector per second. Digital photon counting techniques (such as scintillation detectors and proportional counters), which are able to detect each incident x ray, are not used because they saturate for count rates ~ 10^4 to 10^6/sec and therefore cannot take advantage of the high flux of photons at synchrotron radiation sources (> 10^8 photons per second).

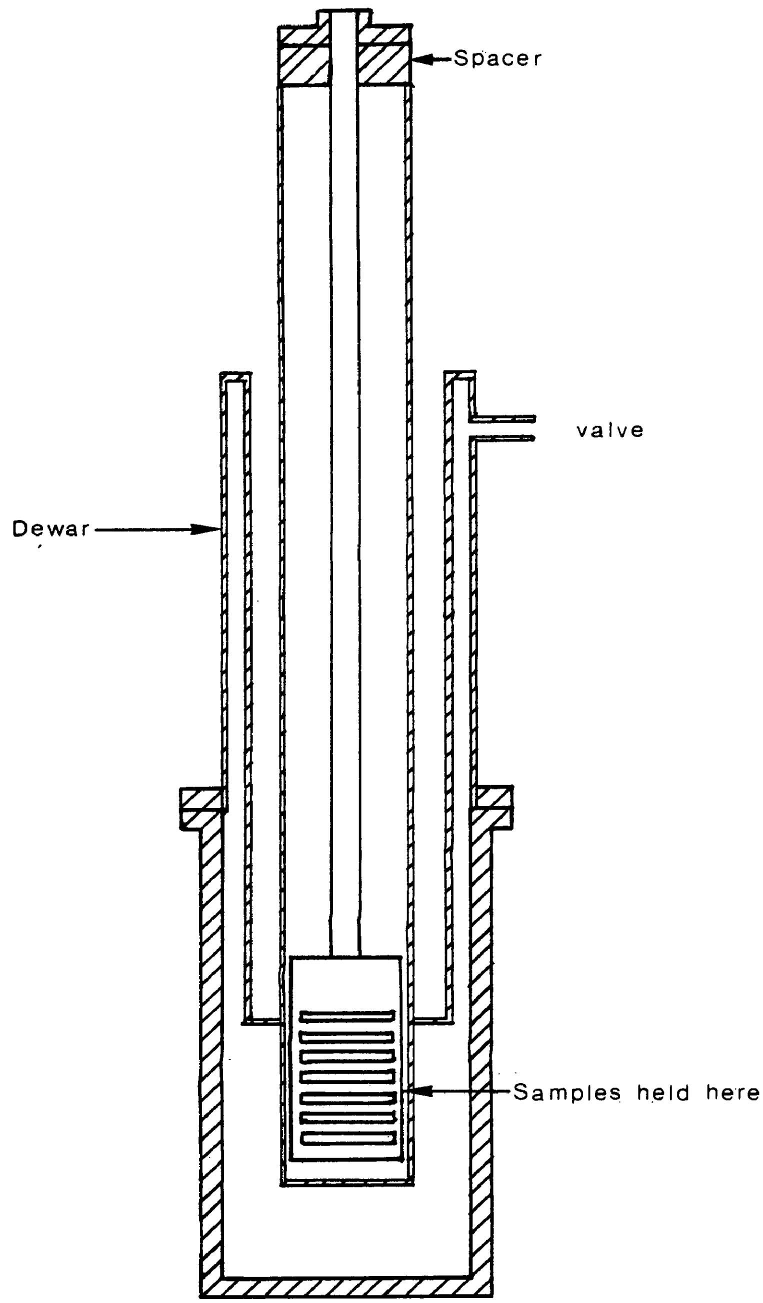

Figure 3.4 Cross Section of Sample Holder/Dewar.

This high flux is necessary, as described above, for achieving large enough S/N for fluorescence-detection experiments. Ionization detectors do not saturate for the high photon fluxes found in synchrotron radiation. The properties of ionization detectors are discussed further in Chapter 4.

Experimental Procedure

Before any x-ray absorption spectra can be measured, several tasks have to be performed. The monochromator is first calibrated in energy using a Sn standard. Then the beam position is determined and the sample table adjusted to give the maximum intensity at the sample. This is done by first adjusting the sample table height to yield the brightest spot on a phosphorescent screen placed at the position of the sample. Then finer adjustments are made by exposing x-ray sensitive Polaroid film to the beam at the position of the sample.

In addition, before each sample is measured, x-ray sensitive Polaroid film is exposed to the transmitted beam. These photographs are used to detect pinholes and low density regions and to check the alignment of the sample in the sample holder. The x-ray beam passes through pinholes and is only slightly attenuated through low density regions. Any movement of the beam during an experiment will expose different areas of the sample, changing the number of absorbing atoms and the intensity of the EXAFS signal if the sample is inhomogeneous. Low density regions will also increase the magnitude of the background signal and causes a problem in the normalization of $\chi(k)$, as noted above for higher harmonics. Pinholes and low density regions are eliminated where possible by placing lead over these spots. The samples measured for this project are very uniform and no pinholes were detected.

Once these steps are taken, the experimenter chooses the energy range for the spectrum, the energy increment between data points, and the amount of time for which the computer will count at each of these points. The computer then controls the data acquisition. It scans the beam in energy by changing the angle of the crystal monochromator while simultaneously changing the height of the sample table to keep the x-ray beam directly on the sample. Both are controlled by means of stepper motors. It records the position of the monochromator (in stepper motor steps which have a one-to-one correspondence with energy), the intensities of the initial, transmitted, and fluorescent signals, and counting time in seconds. The intensities are determined by converting the ionization chamber current to voltage and then by counting the pulses generated by the voltage-to-frequency converter and dividing by the counting time. This gives a value proportional to the energy flux, the intensity of the beam. When the run at SSRL is completed, all spectra are transferred from the PDP-11 computer hard disk onto magnetic tape, each experimental scan being stored as an individual data file. Once back at CSM, the data files are transferred to the Gould 9750A computer and stored in the appropriate form for data analysis.

Chapter 4
DETECTOR FOR FLUORESCENT X-RAYS

Properties of Ionization Detectors

An ionization detector consists of a chamber filled with a gas and containing two electrodes held at a certain potential with respect to each other. When an x-ray enters the chamber, it will ionize the gas atoms or molecules, producing electron-ion pairs. For argon gas (Ar), ~30 eV is required per electron-ion pair. The response of an ionization detector is dependent upon the type of filling gas, the geometry of its construction, the applied voltage and the intensity of the incident radiation. For small values of the applied voltage across the two electrodes, the electrons and ions recombine before reaching the electrodes. If this voltage is greater than a certain voltage, V_i, then electron-ion recombination is kept to a minimum and each is collected by its appropriate electrode. A current is then produced in the external circuit of the detector which is independent of the applied electric field. This mode of operation of the gas ionization detector is known as the ionization chamber region of the gas chamber response curve (Figure 4.1) [20]. V_i is typically 30 to 100 V and is dependent upon the geometry of the chamber, the filling gas, and the intensity of the incident radiation. The current produced is proportional to the product of the number of x-ray photons absorbed by the gas in the chamber with the energy of these photons. If the applied voltage is increased

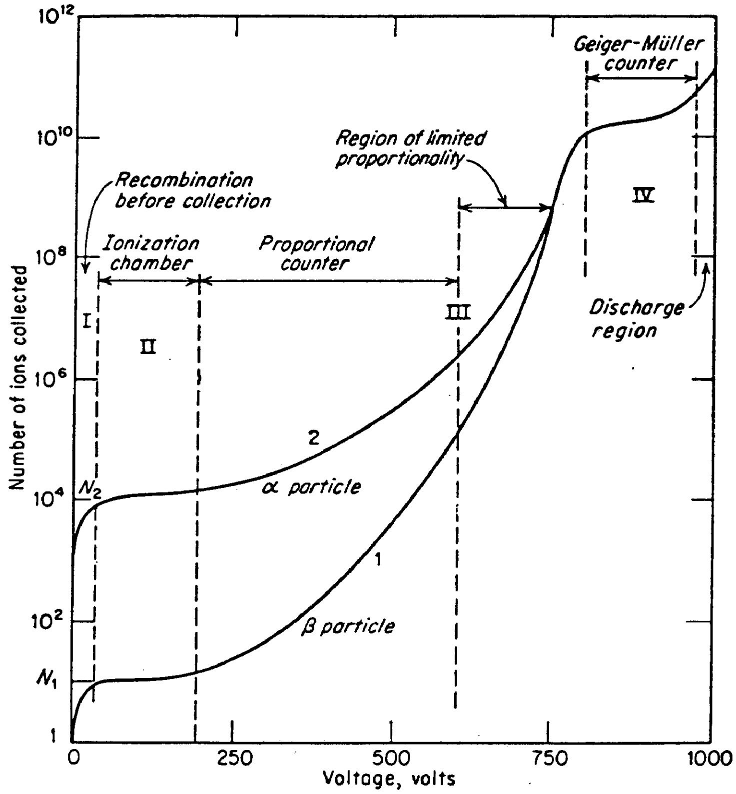

Figure 4.1 Gas Ionization Detector Response Curve (20). Used to illustrate the response of ionization detectors.

further, the electrons and ions will acquire enough kinetic energy to ionize other gas molecules through collisions as they move towards the electrodes, thus multiplying the signal. The resulting current pulse is proportional to the initial ionization with a multiplication factor which is proportional to the applied electric field. This part of the detector response curve is called the proportional region because the current pulse produced by one photon is large enough to be measured and is proportional to the energy of the x-ray photon.

To measure the incident intensity of the x-ray beam, an ionization chamber 15.2 cm in length filled with Ar is placed in the path of the x-ray beam before it strikes the sample (corresponding to ion chamber 1 in Figure 3.1). Ar is used in this chamber because it absorbs very little of the beam (its absorption length is 234 cm at the Sn K-edge, 29.2 keV). For transmission experiments, another ionization chamber 30.5 cm in length, again filled with Ar, is placed behind the sample along the beam axis (corresponding to ion chamber 2 in Figure 3.1). This measures the intensity of the beam after it passes through the sample (i.e., the transmitted intensity). The current signals from each of these detectors are then amplified and passed through current-to-voltage and voltage-to-frequency converters before being passed to the computer for recording.

For fluorescence-detection experiments, an ionization chamber filled with krypton gas (Kr) is placed at 90° to the beam in the plane of the synchrotron on a platform upon the frame supporting the sample holder/dewar (corresponding to ion chamber 2 in Figure 3.1). The position is chosen to minimize the contributions to the background by both inelastically and elastically scattered radiation from the sample and the sample holder. This is effective because Compton scattering has a minimum in intensity at 90° to the incident beam in the plane of the synchrotron [21]. The sample normal was then fixed at 45° to the incident beam in order to minimize the attenuation of the fluorescent x rays as they leave the sample in the direction of the fluorescence detector. The fluorescence detector was built at CSM specifically for these experiments to detect, amplify, and convert to voltage the small fluorescence signal. This signal was then passed through a voltage-to-frequency converter and finally to the computer as described above. This detector consists of two distinct parts: an ionization chamber and an amplifying current-to-voltage converter (Figure 4.2).

Ionization Chamber

The ionization chamber is made from 2 mm thick aluminum sheet bent and then welded into the form of a rectangular box of approximate dimensions 15 cm in length by 18 cm in height by 11 cm in width. Its front window, transparent to x rays, is made from 100 μm thick aluminized mylar. The back wall is 6 mm aluminum plate and separates it from the electronics. The interior contains five electrodes of approximate dimensions 15 cm in height by 10 cm in width separated from each other by a distance of 2.5 cm (Figure 4.2). Four of these (plates 1 through 4) are constructed of aluminized mylar (25 μm thick) attached

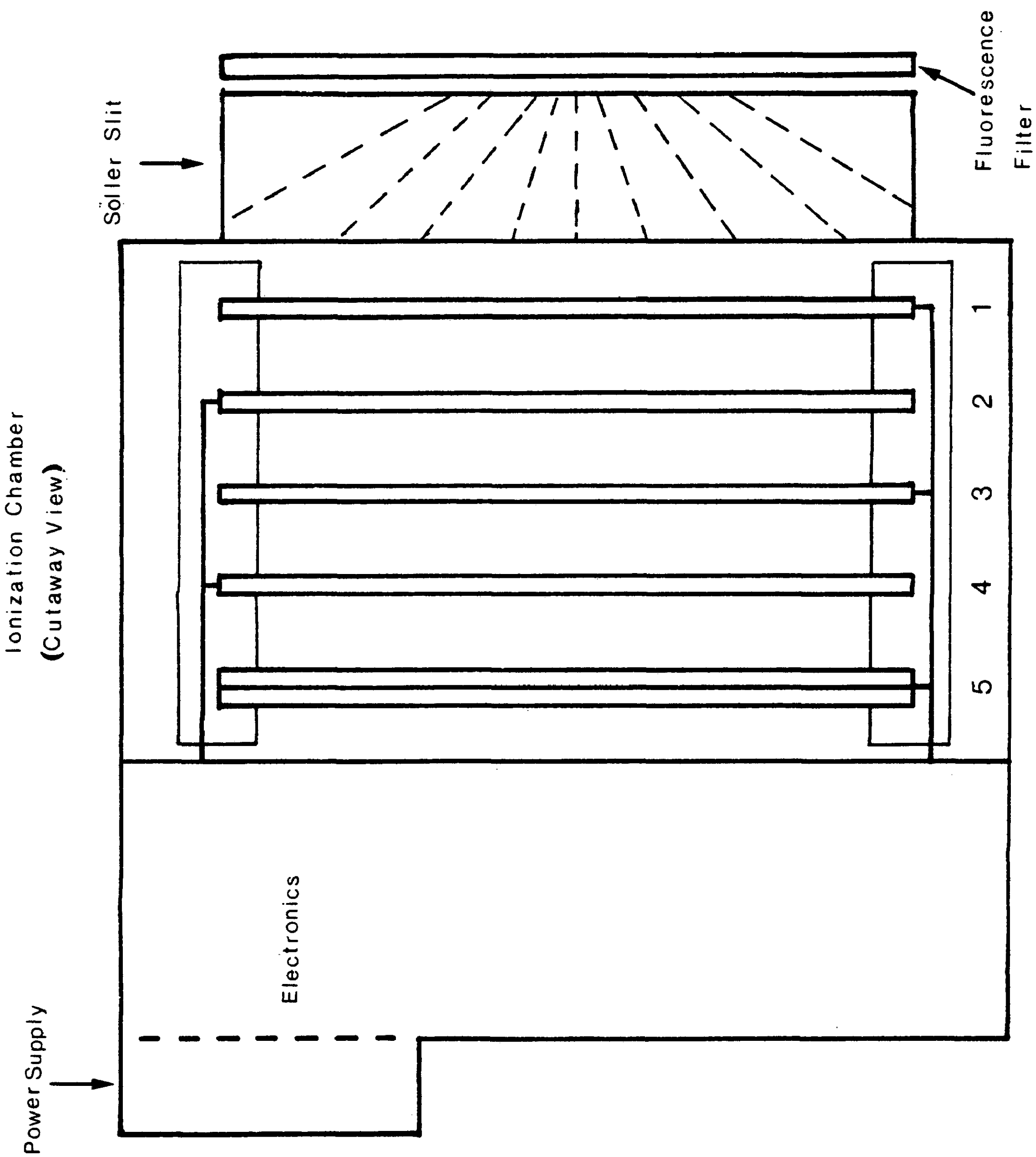

Figure 4.2 Ionization Detector for Fluorescent X Rays.

to 3 mm thick aluminum frames by epoxy. Plate 5 is a solid 3 mm aluminum plate backed with a 2 mm lead sheet to shield the electronics from x rays. The two outer plates and the center plate (plates 1, 3, and 5) are shorted together as are the two intermediate plates(plates 2 and 4) to form the two plates of a capacitor. These plates are designed to transmit x rays so that most absorption will take place in the gas. They are insulated from each other and held rigid by Teflon blocks. They are insulated from the box by Teflon sheet. Teflon was chosen as the insulator because of its extremely large surface resistance when degreased (see below). This large resistance is essential, as described below, for the proper operation of the detector [22]. Plates 1, 3, and 5 are held at a potential of -45 volts relative to the plates 2 and 4 and the box. It was measured that $V_i \sim 25$ V for this detector and therefore at 45 V it is in the ionization chamber region of the gas ionization detector response curve (Figure 4.1).

As described above, the signal resulting from fluorescence EXAFS is very small. In making fluorescence measurements, therefore, the background signal should be made as small as possible and the signal from the fluorescing atoms of interest in the sample as large as possible. The background signal is caused by both elastic and inelastic scattering of the incident beam and fluorescence from atoms other than the element of interest. It is generated both in the sample and from other sources such as the sample holder. It is reduced through the use of a Söller slit and fluorescence filters (Figure 4.2). The fluorescence filter, placed between the Söller slit and the sample, is used to absorb most of the elastic and Compton scattered radiation from the incident beam. It also absorbs most fluorescent x rays originating from atoms with atomic number, Z, less than that of the element of interest. The filter for Sn (Z=50) was made out of silver (Z=47). The Söller slit eliminates a large fraction of the fluorescent x rays from the filter. It is made from lead coated aluminum vanes inside an aluminum frame. The vanes are arranged in such a way as to provide a clear path into the ionization chamber for those x rays emanating from a line source at the sample, while effectively blocking most x rays which do not originate at the sample. If these screening mechanisms work, then most radiation entering the ionization chamber is from the atomic species of interest.

To make the signal from the fluorescing atoms as large as possible, Kr was used as the absorbing gas in the chamber. The absorption length (the inverse of the absorption coefficient) of an x ray at the K_α energy of Sn (25.3 keV) in Kr is 10 cm, while that of Ar is 151.9 cm. Since the length of the ionization chamber is ~15 cm, Kr will absorb most of the x rays, which will result in a larger signal.

Electronics

The first stage of the electronics of the ionization detector uses an AD310K Varacter Bridge Operational Amplifier (opamp) manufactured by Analog Devices [22]. In its current amplification/voltage conversion arrangement with $R_f = 10^{10}\,\Omega$ (Figure 4.3), it converts 0.1 nanoamp

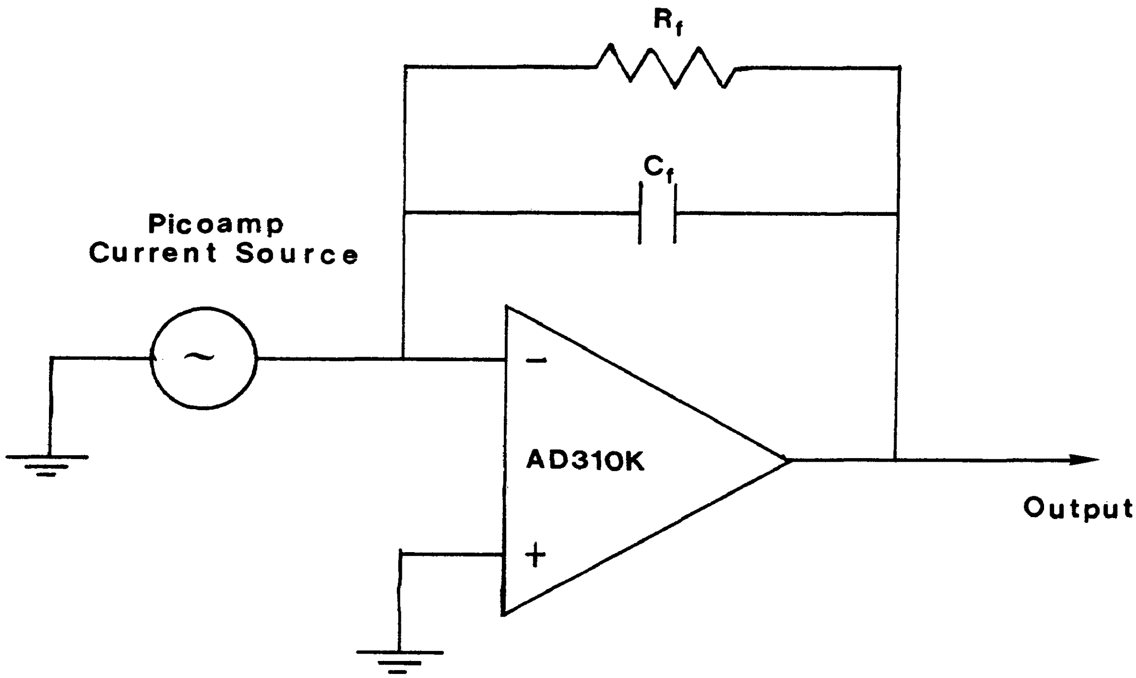

Figure 4.3 Ultra-Sensitive Current Amplifier Schematic [22].

current to one volt. Typically, the signals from the ionization chamber are in the picoamp to femtoamp range. Therefore, a second stage using another opamp amplifies the signal by factors of 1, 10, 100, or 1000 to increase the output signal from the AD310K to the same order as the other ionization chambers used in the experiments (~0.1 to 1.0 V).

Problems Encountered

When the ionization detector was first built (1/87), it was put together under time pressure and hence had several problems in its design and construction which were not discovered until at SSRL. Two of these were electronics problems which were fixed at SSRL. The additional problems were a very large DC offset in the quiescent signal, a longtime capacitive decay in this signal, and microphonic noise. In order for the detector to perform properly, these problems had to be fixed.

DC Offset. Due to the extremely large value of the feedback resistor ($10^{10}\,\Omega$), any leakage path between the output and the inverting input of the opamp with resistance less than $\sim 10^{14}\,\Omega$ will cause a signal in the opamp. This is specified in the manual of the AD310K [22] and was the cause of the large DC offset. This offset was so large that while at SSRL (1/87), the offset of the detector could not be zeroed or made positive. Since the computer only accepts positive offsets, a 1.5 V battery had to be inserted between the detector and the voltage-to-frequency converter to correct this problem.

After returning from the 1/87 run, the resistance between the two plates measured with an electrometer was found to be $5 \times 10^{12}\ \Omega$, which is clearly less than the acceptable limit. These problems were corrected by installing the proper mounting socket for the AD310K, which had Teflon insulated contacts, by rebuilding and then thoroughly cleaning the Teflon pads which insulate both sets of plates from each other and the box, and by installing Teflon O-rings, where previously rubber O-rings had been used, around the electrode feed-throughs from the ionization chamber. The resistance between the inner and outer diameters of the rubber O-rings was measured to be $10^{12}\ \Omega$, while that of the Teflon O-rings was $>10^{13}\ \Omega$. In addition, a ceramic switch was installed and all exposed wire in the circuit was covered with Teflon tubing.

The Teflon was degreased in the following manner. Within an ultrasonic cleaning chamber, the Teflon parts (plate holders, sheets for the chamber walls, and O-rings) were placed in organic solvents for fifteen minutes in the following order: trichloroethylene to remove all grease; acetone to remove the trichloroethylene; methanol to remove the acetone. The parts were then dried off with dry gas to minimize adsorption of water vapor. At all times, gloves and tweezers were used to handle these parts.

Microphonic Noise. Another problem found with this detector was that of microphonic noise. Microphonic noise, as its name implies, arises from sound vibrations producing signals in the circuit. This had its source in both the ionization chamber and the electronics. Due to the construction of the plates (as described above) the ionization chamber is particularly sensitive to sound vibrations. Any vibration of the plates changes the capacitance of the detector. Since the plates are at a constant potential, this results in a time-dependent (oscillatory) current between the plates of the detector which is picked up by the opamp as a signal. After the 1/87 run, the detector was disassembled. It was found that the aluminized mylar sheets had not been stretched tightly across the frames and the electrodes were not rigidly fixed by their holders. This was corrected by stretching the mylar very tightly before epoxying it to the frames and by rebuilding the Teflon plate holders so that the plates were held rigidly. The mylar was stretched tightly on a board covered with foam rubber which provided pressure to keep the mylar taut. The frames were then epoxied to the mylar while the tension was maintained. The Teflon plate holders were designed to make contact with the entire top and bottom edge of the plates. The previous ones held the plates only over a fraction of their width. The placement of Teflon sheet on the walls of the chamber made the fit between the plates and the walls extremely tight; the plates were effectively immobilized.

The microphonic noise in the electronics was generated by loose wires moving in response to external vibrations. Due to the extreme sensitivity of the current amplifier, any movement of circuit components can generate extraneous signals because this changes the capacitance.

The manual of the AD310K opamp specifies that all components be held rigid for optimum performance [22]. When the circuit was rebuilt, all leads were made as short as possible and were rigidly fixed, if necessary, to the circuit board.

<u>Capacitive Time Constant</u>. The probable cause of the long capacitive time constant in the quiescent signal was the existence of insulating surfaces on the plates and on the interior surface of the box. The entire inner surface of the chamber window and the outer surface of plates one and four were bare (non-aluminized) mylar. Charge will accumulate on these non-conductive surfaces, reducing the net electric field between the plates and therefore the electron collecting ability of the detector. When the detector is first connected to a power supply, charge begins to collect on these non-conductive surfaces. This charging of a capacitor has a certain RC time constant. To prevent this charging, The largest areas (those mentioned above) were replaced with aluminized mylar and the inner surface of the window was grounded to the box. Any other insulating surfaces on the plates (such as exposed epoxy) were painted with conductive silver paint. The elimination of these surfaces reduced these decays to a minimum. Before these changes had been made, it took the detector ~2.5 days to reach a steady state value after the power supply was turned on. After, it took ~1.0 hours for this to occur.

Additional Refinements

Other improvements were made to the detector which had minor effects upon its performance. A new power supply was installed, mounted directly upon the rear of the detector with shielding grounded to the detector case (Calex model 22-100). This eliminated the necessity of an external power supply and the additional microphonics which would be generated in the wires connecting it to the detector. A switch was installed on the battery so that it could be disconnected from the plates when not in use. The rear of the case was made removable to give easier access to the electronics for any servicing which might need to be done.

Resultant Performance

The 12/87 run verified that the aforementioned changes had in fact improved the performance of the detector. Figure 4.4 shows the difference between the 1/87 run and the 12/87 run for Al Sn 10ppm. The signal-to-noise was improved considerably due largely to the addition of external shielding (described below) and the changes mentioned above. In the 12/87 run, EXAFS can clearly be seen.

In the 12/87 run, it was found that x rays from non-sample fluorescence in the hutch were entering the detector through its walls and were therefore being detected. To prevent x-rays from entering the ionization chamber in this manner, the exterior surfaces of the ionization chamber were covered with lead sheet. This reduced the background signal by about a factor of ten. This turned out to be very important for the resolution of the EXAFS for the more dilute samples analyzed. After the background signal was reduced to as small a value as possible, the elimination of other sources of noise, described above, became important. The difference in step height in the spectra (0.4 vs. 0.04) is caused by a different setting of the fluorescence detector gain (10X) in January 1987.

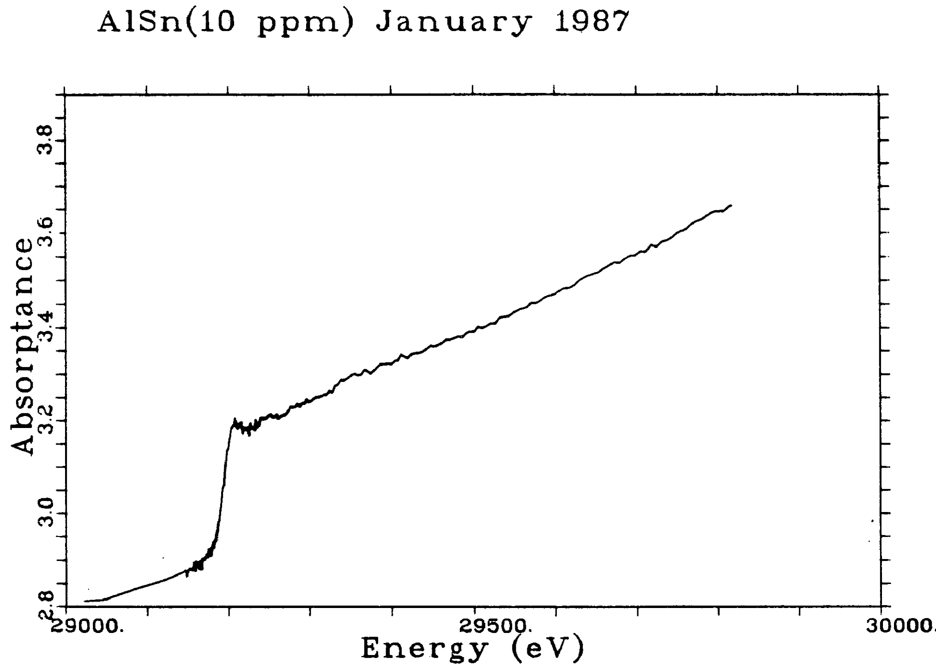

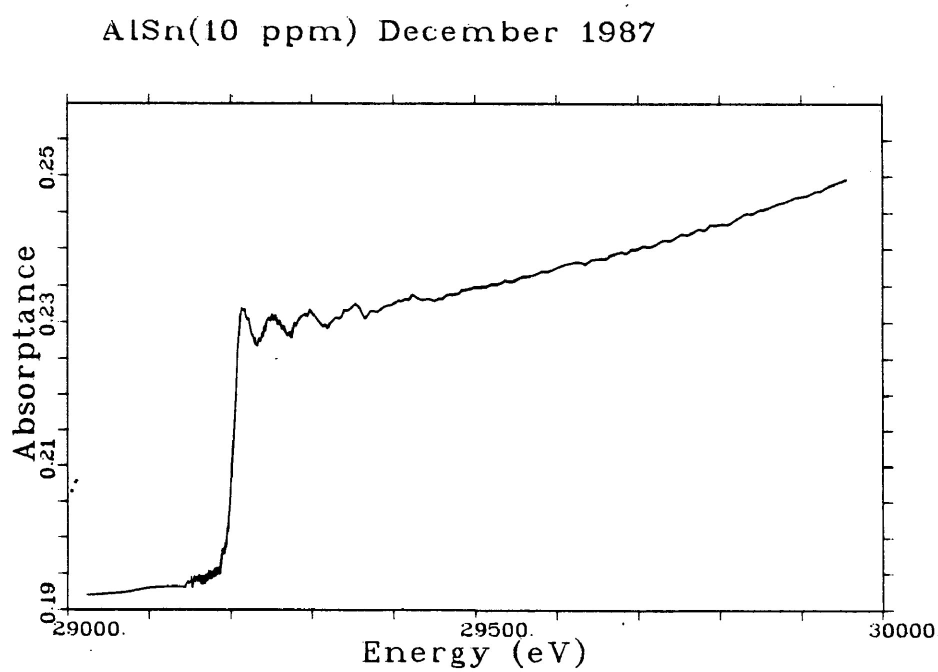

Figure 4.4 Comparison of AlSn:10 ppm from January 87 and December 87.

Chapter 5
DATA ANALYSIS

There are several steps which must be taken in the data analysis in order to extract the structural information contained in the EXAFS:

- Single-point spikes in some of the data files must be corrected.
- The S/N of the data must be maximized by adding together sets of data files.
- $\chi(k)$ must be extracted from the x-ray absorption spectrum.
- $k\chi(k)$ must then be Fourier transformed to separate the peaks in r-space.
- Fits must then be made between the spectrum being analyzed and calculated spectra and/or standards in r-space, k-space or both.

Correcting Small Errors in the Data

One of the problems encountered upon examining the data of the dilute alloys and other data from SSRL was that of occasional irreproducible events in the data. These were of two forms, spikes and sudden shifts in the intensities, commonly called "glitches" [17]. Spikes are large sudden increases or decreases in one of the beam intensities possibly due to electrical malfunctions in one of the detectors. They usually consisted of a single data point which was corrected by taking the average of the two adjacent data points and substituting this value for the spike value. The spectra containing spikes were corrected and then included in the data analyzed.

The probable cause of glitches is electrons in the ring moving out of alignment and changing the spectral characteristics of the synchrotron radiation. This showed up in the spectrum after taking the appropriate ratio because either the detectors did not respond linearly to the shifts or the shifts induced changes in the relative concentrations of primary and higher harmonics, which has the most effect upon the transmitted and fluorescence intensities. Since the effect that caused these shifts is not well understood, the spectra which contained glitches were not used in the data analyzed.

<u>Increasing the Signal-to-Noise Ratio</u>

To increase the S/N of the fluorescence-detection spectra, all spectra of the same sample which were free from the errors described above were added together. First, the edge energy of each spectrum to be added was determined by the method described below. Then each spectrum was shifted in energy so that all edge energies were equal. The intensities from the spectra were then added up and the appropriate ratio taken (depending upon whether it was transmission or fluorescence). This process is equivalent to taking data for a longer time at each energy (n times as long, where n is the number of data files added) and reduces the random noise, but not the systematic noise. After this process was completed, the S/N was increased by a factor of $\sqrt{n}$ at most. The samples analyzed and the number of files added for each are shown in Table 5.1.

Table 5.1 Data Files Added for the Samples Analyzed

Sample	Method	Number of Files
β-Sn, 12/87	Transmission	1
AlSn(50 ppm), 12/87	Fluorescence	6
AlSn(10 ppm), 12/87	Fluorescence	12
Al ion-implanted with Sn, 12/87	Fluorescence	2

Extraction of $\chi(k)$

By looking at the expression for the x-ray absorption coefficient, we can see the steps which need to be taken to extract $\chi_a(k)$.

$$\mu_s(E_x) = \mu_{bg}(E_x) + \mu_a^o(E_x)[1 + \chi_a(E_x)] \tag{5.1}$$

The usual method for extracting $\chi_a(E_x)$, which works for transmission spectra, is to subtract $\mu_{bg}(E_x)$, divide by $\mu_a^o(E_x)$, and subtract 1 to give $\chi_a(E_x)$. The energy is then converted to k by Equation (2.1) and $k\chi_a(k)$ is the result.

This method of extracting $\chi(k)$ was not used, however, in the analysis of the data described here. It does not normalize fluorescence data properly. In addition to the absorption of the x-rays which takes place in the sample, absorption also occurs in the detectors which is not taken into account. This introduces other energy-dependent terms into equations (2.7) and (2.9). For transmission spectra, these terms are slowly varying functions of energy which are easily removed in the subtraction of $\mu_{bg}(E_x)$. For fluorescence-detection spectra, however, absorption in the fluorescence filter and in the detector itself are strong functions of energy and cannot be removed easily. To account for this effect, $\chi_a(k)$ was extracted from the fluorescence-detection data in the following manner.

First, the edge height, S_0, and the edge energy, E_0, are determined by fitting the spectrum above and below the absorption edge and finding the position where the average of these two fits intercepts the absorption edge. The energy value of this intercept is E_0 and the difference between the two fits at this energy value is S_0. Then the region above the absorption edge is fit with a polynomial in k of order 7 to 10 in order to eliminate the highly energy-dependent terms spoken of above. This fit is then subtracted from $\mu_s(E)$ and the resultant divided by S_0, yielding χ_a. In principle, E_0 is approximately the Fermi energy of the material. Due to many different effects, which include the calibration of the crystal monochromator, E_0 cannot easily be set to a certain value from fundamental considerations. We determined it as above for each spectrum analyzed.

<u>Fourier Transform</u>

After $k\chi(k)$ has been determined, the next step is to Fourier transform this quantity to separate the peaks in $p_{ab}(r)$. 2k and r are used as complementary variables (see equation (2.5)). Due to the finite extent of the data in k space, a window function must be employed in the transform. The type of window function used for this analysis is a square window convoluted with a Gaussian of half-width σ_G. Broadening the window in k-space results in greater localization of the peaks in r-space. In transforming the data, the first 1 to 2 $Å^{-1}$ must be excluded from the data being transformed. In this region, different effects occur which are not taken into account by the theory used for this analysis. The assumption of this theory is that only single scattering events contribute to the final state electron wave function and hence the EXAFS. At these low values of k, however, the electron mean free path is much longer than at higher values (10 to 20 Å at 10 eV versus 5 to 10 Å at 50 to 150 eV) [17]. Scattering is also more isotropic at lower energies. This means that multiple scattering effects make a greater contribution to the scattering signal in this region. In addition, chemical bonding effects come into play and resonances often occur in the cross section at or near the absorption edge. The upper limit in k of the transformable data is determined by the range of experimental data and is usually the point where the EXAFS is on the order of or smaller than the noise.

Extraction of Structural Information

At this stage there are two ways to proceed. The first is to compare the Fourier transform of the spectrum being analyzed with that of experimental standards or calculated spectra in r-space and fit the latter to the former using the program described below. The second is to back-transform part of the r-space data (such as the nearest-neighbor peak) into k-space and compare the amplitude and phase of this data with the scattering amplitude and total phase of tabulated spectra or experimental standards. If the contributions from neighboring shells do not overlap in r-space, then a k-space fit may be used to fit the data. On the other hand, if overlap does occur, the most convenient method of fitting is in r-space. In comparing the Fourier transforms (and back transforms) of different spectra, it is necessary that the same window function be used in all transforms (otherwise, their peak function will be different). For the data analyzed here, the both of these methods were used to extract the structural information from the EXAFS spectra.

Generation of Theoretical Spectra. Calculations have been done which enable relatively easy generation of approximate theoretical $k\chi(k)$'s for many atomic environments [23 to 29]. These are based upon a parametrization of the equation for $\chi(k)$:

$$\chi(k) = \sum_j N_j \, F_j(k) \, \exp\{-2\sigma_{DWj}^2 k^2 - 2r_j/\lambda\} \frac{\sin[2kr_j + \phi_j(k)]}{kr_j^2} , \qquad (5.2)$$

where the sum is over atomic shells of species j around the excited atom of radius r_j containing N_j atoms with mean-square-relative-displacement σ_{DWj}, back scattering amplitude $F_j(k)$ and total phase shift $\phi_j(k)$ given by

$$\phi_j(k) = 2\delta_a^{l=1}(k) + \phi_b(k) - \pi, \qquad (5.3)$$

where $\delta_a^{l=1}$ is the l=1 phase shift of the excited atom, and ϕ_b is the phase of the backscattering amplitude from the neighboring atom. Equation (5.2) assumes that the peaks in p_{ab} are Gaussians. The values of the parameters, $F_j(k)$, $\delta_a^{l=1}(k)$, and $\phi_b(k)$, are tabulated in the articles for selected values of k. To obtain continuous functions of k, they are fit with cubic splines.

The first group to publish these scattering parameters was Teo et al. [23,24] and Teo and Lee [25]. McKale et al. [26 to 29] later published refinements of these. Teo and Lee [25] based their calculations upon plane wave scattering theory. It was thought that this treatment, the "small atom" approximation, was sufficient for describing the outgoing electron wave. Their tabulations have a low-k cut-off at the relatively large k value of 3.8 $Å^{-1}$ because, at the time, it was suspected that multiple-atom scattering became important for smaller values of k. Since then, it has been shown that single scattering theory can be applied to within 20 eV ($k = 1.5$ $Å^{-1}$) of the absorption edge provided that the full curved wave theory is used [26 to 29]. This results in the backscattering amplitude and phase shift being dependent upon r_j. McKale et al. [29] published tabulations of these curved wave backscattering parameters, analogous to those of Teo and Lee [25]. These were given at r_j values of 2.5 Å and 4.0 Å for values of k between 1.5 $Å^{-1}$ and 20.0 $Å^{-1}$. The backscattering parameters for other r values were determined by linear interpolation in 1/r in complex space. For the data analyzed in this thesis, the backscattering parameters of McKale et al. were used in calculating spectra.

Fitting Spectra. There are several steps needed to fit a calculated spectrum to the experimental data in r-space. First, using the electron mean free path, λ, and the relative mean square displacements, σ_{DW}, as adjustable parameters, a $\chi_c(k)$ which resembles the experimental $\chi_a(r)$ is generated. The Fourier transform of this calculated spectrum is then compared with that of the experimental data over a certain region in r space using a least-squares fitting program. This program broadens the calculated spectrum by convolution with a Gaussian, shifts it in r, and multiplies the scattering amplitude by a constant until a minimum is found in the fit parameter, R, given by:

$$R^2 = (2N)^{-1} \sum_{N} \left(\frac{[\mathrm{Re}(\varphi - \varphi_c)]^2}{(\mathrm{Re}\ \varphi)^2 + (\mathrm{Re}\ d\varphi/dr)^2} + \frac{[\mathrm{Im}(\varphi - \varphi_c)]^2}{(\mathrm{Im}\ \varphi)^2 + (\mathrm{Im}\ d\varphi/dr)^2} \right) \quad (5.2)$$

φ_c is the calculated spectrum with the changes induced by the program. The sum extends over all points of the structural feature being fit, in this case the first peak in φ. A fitted spectrum with a value of R <0.01 is virtually indistinguishable from the data. After this first fit is done, it is often necessary to adjust λ and σ_{DW} further to get a better fit. In addition, E_0 must also be adjusted to correct for the inadequacies of the calculation. Once the best fit has been found in adjusting all the parameters, both the fit and the experimental spectrum are often transformed back into k-space to compare their phase and amplitude. If necessary, a linear function of k may be added to the calculated phase shift to bring it into better agreement with the data. Under ideal circumstances, the coordination number can be determined to ~ 5 %, the width of the peak to within 20 % and the scattering distance to less than 1 %.

Chapter 6
RESULTS

Sample Preparation

EXAFS fluorescence-detection experiments were performed on the dilute alloy system AlSn for nominal atomic Sn concentrations of 10 ppm and 50 ppm. The measurements were made on these alloys in two different forms: as-prepared (January 1987 [1/87]) and as-quenched from a high temperature anneal (December 1987 [12/87]). The as-prepared samples were made by melting the appropriate proportions of Al (99.999 % pure) and Sn (99.9 % pure) in a sealed, evacuated quartz tube and quenching the melt to room temperature in water. It was intended that this technique would freeze the Sn in the Al lattice and prevent it from precipitating out or clustering. The resulting pellets were then cold-rolled to a thickness appropriate for EXAFS fluorescence-detection measurements (~ 2 mm) and cut to the correct size for the EXAFS sample holder. Since Sn is soluble in solid Al at 900 K for atomic concentrations less than ~ 200 ppm, it was expected that its distribution would be truly random in these samples. After the data from these samples were analyzed, however, it was found that substantial tin precipitation had occurred in the sample. Further treatment and measurement of these samples was needed. In November 1987, each sample was annealed for 24 hours at 900 K (20 K below the melting point of Al) in a sealed, evacuated quartz tube and then quenched in water to room temperature. The purpose of this second treatment was to allow sufficient time for the Sn to diffuse throughout the sample and disperse randomly in solid solution. The samples were then quenched from a lower temperature than before (which had been above the melting point of Al) in an attempt to freeze the Sn at random sites in the Al lattice, thus hopefully eliminating the clustering which had occurred previously. At the annealing temperature for the time allowed, the average diffusion length, $\sqrt{Dt}$, based on the diffusion coefficient determined by Tiwari and Sharma [30] is 0.2 mm. This gave the Sn atoms more than enough time to disperse in the solid solution. In addition, Sn has its maximum solid solubility in Al at this temperature and hence a lower probability of clustering. After this treatment, grain boundaries and large grains (1-2 mm in diameter), which were not apparent before, were clearly visible to the naked eye. Before the annealing, the Fourier transforms of the samples resembled that of β-Sn, while after this treatment, they resemble Al. The annealing did change the atomic arrangement of the Sn in the samples (as will be discussed below).

In 12/87, fluorescence-detection EXAFS measurements of Al ion-implanted with Sn (5×10^{17} Sn atoms/cm^2) were also made. These samples were prepared by Spire Corporation by implanting 160 keV Sn ions into a 99.997 % pure Al foil (.25 mm thick). The surface of the Al was highly polished before implantation to provide a smooth uniform surface and the Al was affixed to a cooling plate during the implantation. Transmission EXAFS measurements were also made on pure β-Sn foil to provide a standard with which to compare the AlSn data.

Standards

In order to fit the data from the AlSn alloys, it was first necessary to fit experimental Sn and Al spectra separately with calculated spectra. This was done to find the correct scattering amplitude and phase shift for Al and the correct excited atom phase shift for Sn, and to provide an amplitude reference to determine the number of atoms in the first neighbor shell of AlSn. In the process of fitting, E_0 was shifted and a linear function of k was added to the phase. These changes were included in the Al and Sn phase shifts and the Al scattering amplitude before generating a calculated Sn-Al signature (i.e., the signature from an excited Sn atom with an Al backscattering atom).

The experimental β-Sn spectrum was fit in r-space over the range 2.18 to 3.75 Å with four Sn peaks at the positions of the first four scattering shells (radius 3.02, 3.17, 3.76, and 4.42 Å with 4, 2, 4, and 8 atoms, respectively) (see Figure 1.1). E_0 was adjusted by -5 eV to provide a best fit of R = 0.009. $k\chi(k)$ and $\varphi(r)$ for β-Sn are shown in Figure 6.1.

Two experimental Al spectra were provided by P. Lagarde [31]; one was of the spectrum published in Reference 32 which used an organic KAP crystal in the monochromator and the other was a shorter scan of unpublished data which used a quartz crystal in the monochromator (Figures 6.2 and 6.3). The longer scan was used in this analysis in

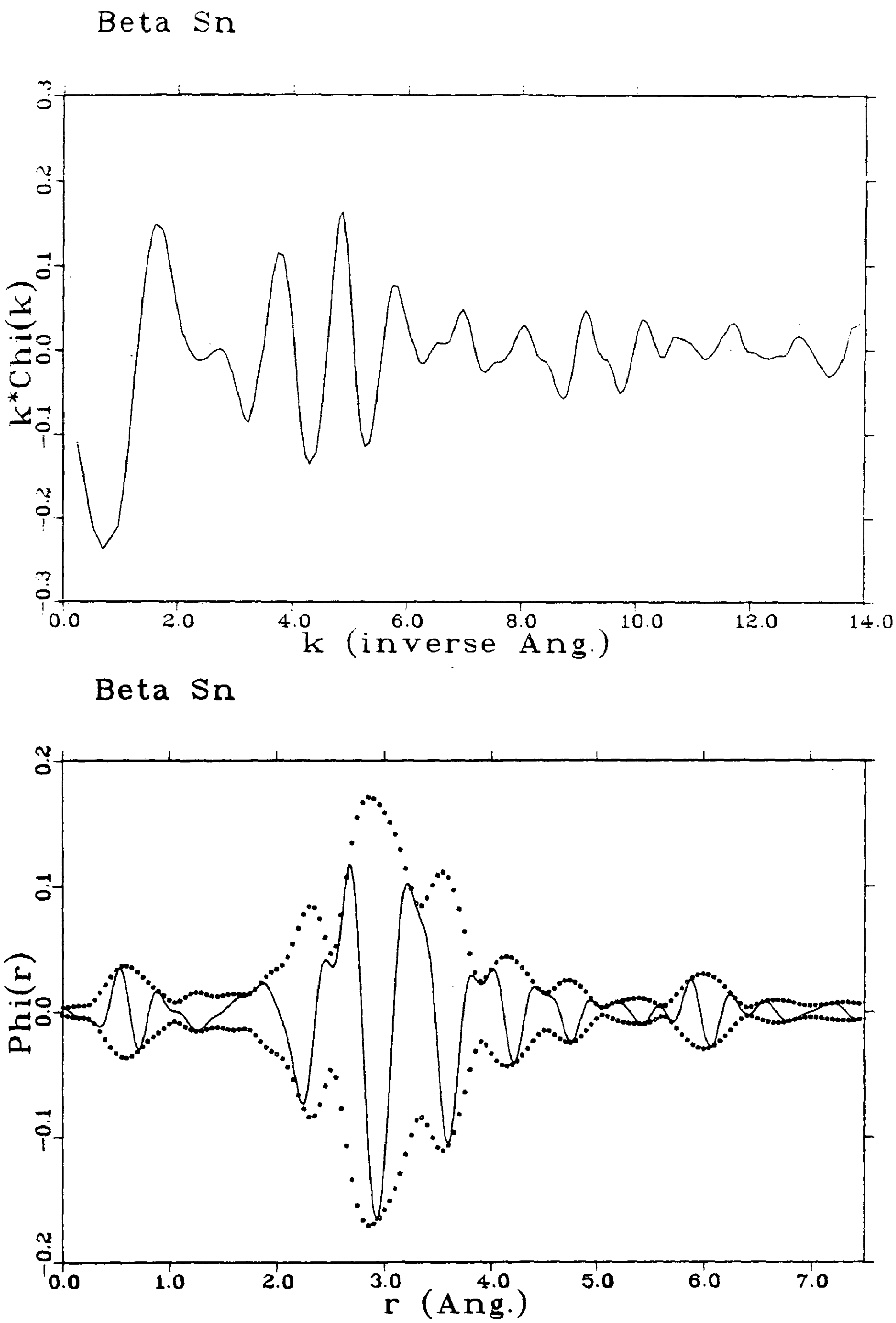

Figure 6.1 $k\chi(k)$ and $\varphi(r)$ for β-Sn.
Transform limits: 2.2 to 13.67 $Å^{-1}$.

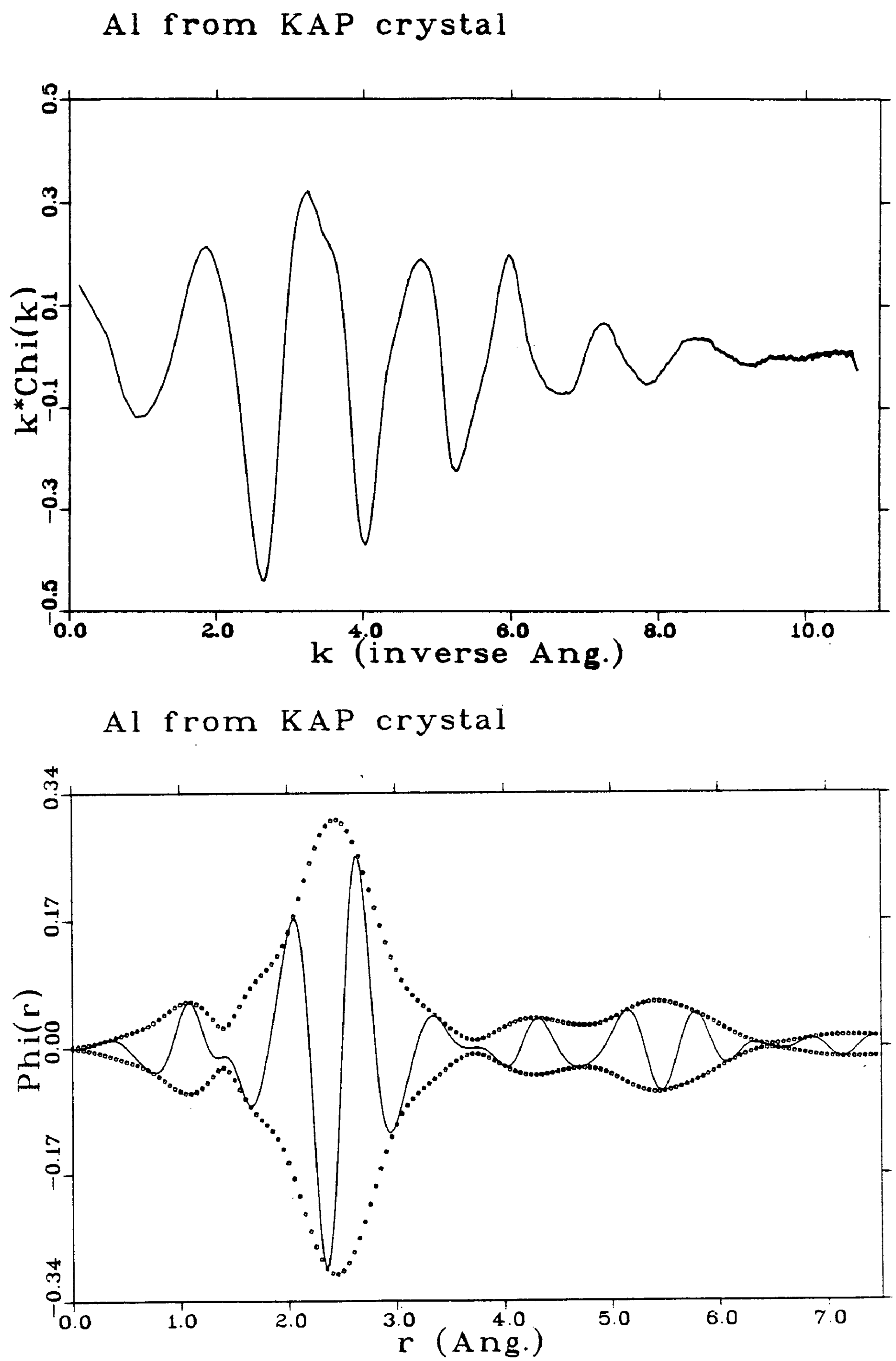

Figure 6.2 $k\chi(k)$ and $\varphi(r)$ for Al from KAP Crystal.
Transform limits: 2.5 to 10.57 $Å^{-1}$.

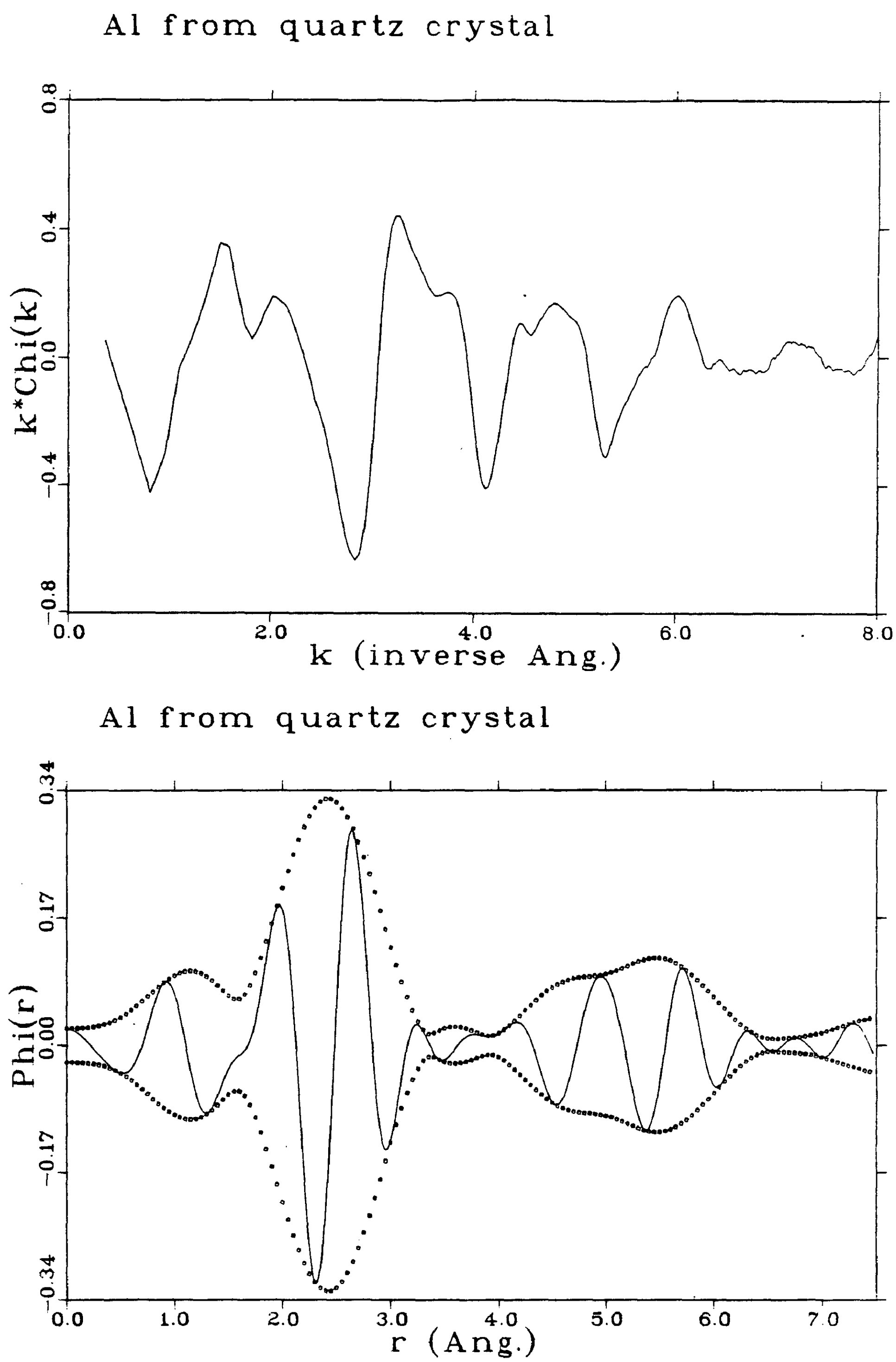

Figure 6.3 $k\chi(k)$ and $\varphi(r)$ for Al from Quartz Crystal. Transform limits: 2.5 to 8.0 $Å^{-1}$.

order to get a more accurate fit. The spectrum was fit over the limits of the first neighbor peak, 1.62 to 3.10 Å, with one Al peak at the Al nearest neighbor (nn) position of 2.864 Å. E_0 was adjusted by -19.25 eV to give a best fit of R = 0.015. In addition, it was found that Al was fit better with two Al Gaussian peaks separated by 0.14 Å, yielding R = 0.011. These two peaks are so close together that their sum is more properly interpreted as a single non-Gaussian peak than as two separate Gaussian peaks. This non-Gaussian peak may represent an interesting structural result for Al or it may simply reveal a shortcoming of the calculated Al backscattering amplitude.

After these fits had been made, the Al backscattering phase and amplitude were adjusted by shifting k by ΔE_0 = -19.25 eV and adding a factor of -0.019k to the backscattering phase. For the Sn excited atom phase shift, k was shifted by ΔE_0 = -3.4 eV and 0.015k was added to the phase shift. The E_0 shift for the Sn in this signature is different from that obtained in fitting β-Sn because the Fermi energy of Sn must be adjusted to match that of Al, the host lattice. The Fermi energy of Al is 1.6 eV greater than that of Sn and so 1.6 eV was added to the Sn E_0. These parameters were then used to generate an Sn-Al signature at r = 3.00 Å. This signature, a Sn-Sn signature, and the experimental β-Sn spectrum were used to fit the <u>Al</u>Sn(10 ppm), <u>Al</u>Sn(50 ppm), and Al ion-implanted samples. The ranges in r-space for the fits of these spectra were chosen by comparison with the fitting signatures and then including the range in which the signatures could give the greatest contributions to the peak in the spectra.

In the tables which follow, $\delta\sigma^2 = \sigma_{sam}^2 - \sigma_{sig}^2$. It is the difference between the square of the half-width of the sample and the square of the half-width of the standard in the units of Å². It gives a measure of the relative widths of the samples and the signatures. Some table entries are marked with an asterisk. If under 'No. of atoms', this indicates that the total number of atoms in the signature (which may be unknown) was multiplied by the value given. If under 'r, Å', then the signature was shifted in r by the amount given.

Findings

AlSn(50 ppm). In February 1987, the AlSn(50 ppm) sample was measured by Mössbauer spectroscopy and it was determined by the resonance signal area that the actual Sn concentration is closer to 70 ppm [33]. $k\chi(k)$ and $\varphi(r)$ for this sample are shown in Figure 6.4. The spectrum was first fit over the limits 1.81 to 2.98 Å which included the main peak. This fit range gives a very good fit with a single Al peak ($R = 0.018$) with 12.7 nn (see Table 6.1). For two Al peaks, a result is obtained which is similar to Al: the peaks are separated by ~ 0.1 Å and the R value is reduced by 0.004. This probably indicates a deficiency in the calculated Al scattering amplitude. This result also gives the nn number closer to 12. The data were then fit with one Al and one Sn peak, yielding 12 atoms again (9 Al and 3 Sn) and approximately the same R value. The ~ 12 nn atoms found in this fit range are consistent with

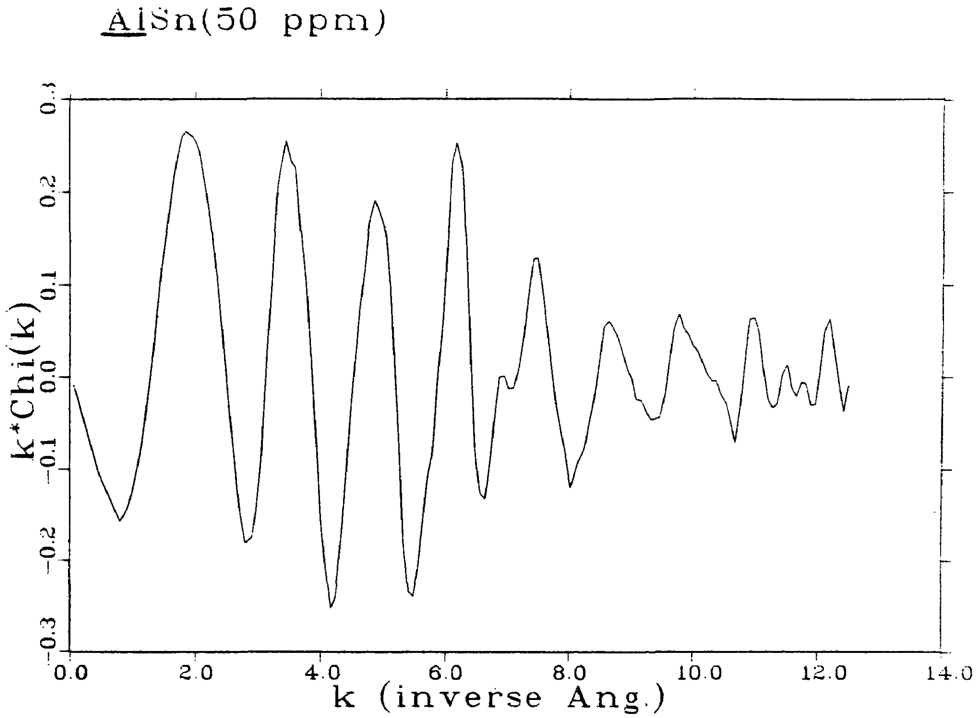

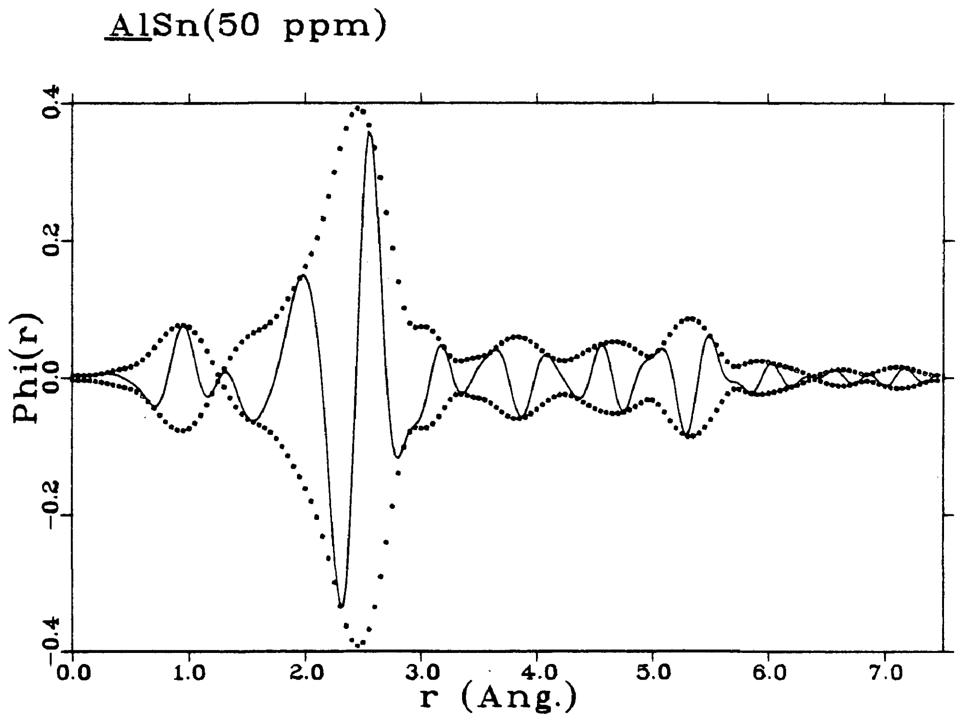

Figure 6.4 kχ(k) and φ(r) for AlSn(50 ppm) from December 1987. Transform limits: 2.5 to 12.33 $Å^{-1}$.

Table 6.1 Fit Parameters for <u>Al</u>Sn(50 ppm).

Signature	No. of atoms	r, Å	$\Delta\sigma^2$, $Å^2$	R
Range: 1.81 to 2.98 Å.				
Sn-Al	12.7	2.97	0.004	0.018
Sn-Al	5.1	2.93	-0.001	
Sn-Al	7.0	3.03	0.002	0.014
Sn-Al	9.0	2.94	0.0002	
Sn-Sn	3.0	3.02	0.008	0.012
Range: 1.81 to 3.28 Å.				
Sn-Al	13.8	2.97	0.005	0.049
Sn-Al	9.6	2.97	-0.0001	
Sn-Al	5.8	3.12	0.006	0.034
Sn-Al	9.2	2.96	0.0002	
Sn-Sn	4.7	3.09	0.014	0.026
Sn-Al	6.1	2.93	-0.005	
Sn-Sn	2.2	3.00	-0.006	
Sn-Sn	3.2	3.15	-0.001	0.021

Sn substitutional in the Al fcc lattice, which is what one might expect. The Sn-Sn distance obtained is 3.02, equal to the nn distance in β-Sn (where there are, however, 4 Sn nn atoms).

Note that the fit with both Al and Sn peaks can be interpreted in several ways since this technique probes the average environment of the Sn atoms: each Sn has 9 Al and 3 Sn nn atoms; 75 % of the Sn atoms have 12 Al nn while 25 % have 12 Sn nn; some combination of these.

Comparing Figures 6.4 and 6.2, the 50 ppm data looks very similar to that from Al metal, with the exception of the feature adjacent to the main peak at ~ r = 3.2 Å. The data were also fit over the range 1.81 to 3.28 Å to include this feature. The signatures which could give rise to such a feature are Sn-Sn and β-Sn and thus it was suspected that Sn precipitation was the cause of this. This assumption was supported by the fits that were obtained. For this range, the fit with one Al and one Sn peak is considerably better than the fit with two Al peaks. The fit with β-Sn, however, gives nonsensical results and is not reported. These fits found ~ 14 nn, which suggests that more than two peaks are needed to explain this larger range. This range was then fit with one Al and two Sn peaks. This gives a good fit (R=0.021), with a total of 11.5 nn, ~ 6 Al atoms and ~ 6 Sn atoms. The Sn atoms are at approximately the positions of the first and second nn in β-Sn which may indicate Sn precipitation.

For the 50 ppm sample the following has been determined. When the spectrum is fit over the range of the main peak, an excellent fit with ~

12 nn is obtained, which could consist of either Al alone or a combination of Al and Sn. Over the larger range, fits with a single Al peak, two Al peaks, and one Al peak with one Sn peak give ~ 14 nn, which is not consistent with the fcc structure. A better fit is obtained with one Al and two Sn peaks, which again gives 12 nn and supports the existence of Sn precipitates. The structure of this sample then appears to be composed of Sn in solution plus Sn precipitates. The exact structure cannot, however, be determined definitely from this analysis alone. The results of the fits are given in Table 6.1.

AlSn(10 ppm). $k\chi(k)$ and $\varphi(r)$ for this sample are shown in Figure 6.5. The Sn concentration in this sample was determined to be ~ 11 ppm from the ratio of the step height of the 50 ppm sample to that of this sample (equal to 6.5). Like the Fourier transform of the 50 ppm data, that of 10 ppm data is very similar in appearance to that of Al, with the exception of a feature above the main peak in r-space. The spectrum was first fit over the range 1.90 to 2.95 Å, which includes only the main peak. For this range, an average of 9 nn were found (see Table 6.2). As can be seen from the fits, the inclusion of other peaks does not improve the fit substantially. The two Al peaks, found separated by ~ 0.1 Å, may indicate a deficiency in the calculations, as noted above. There is no improvement using one Sn peak in addition to one Al peak.

In order to get more information about this structure, the spectrum was fit over the range 1.9 to 3.15 Å, which includes the feature at ~ r = 3.10 Å. As can be seen from the R values, none of the two-peak fits

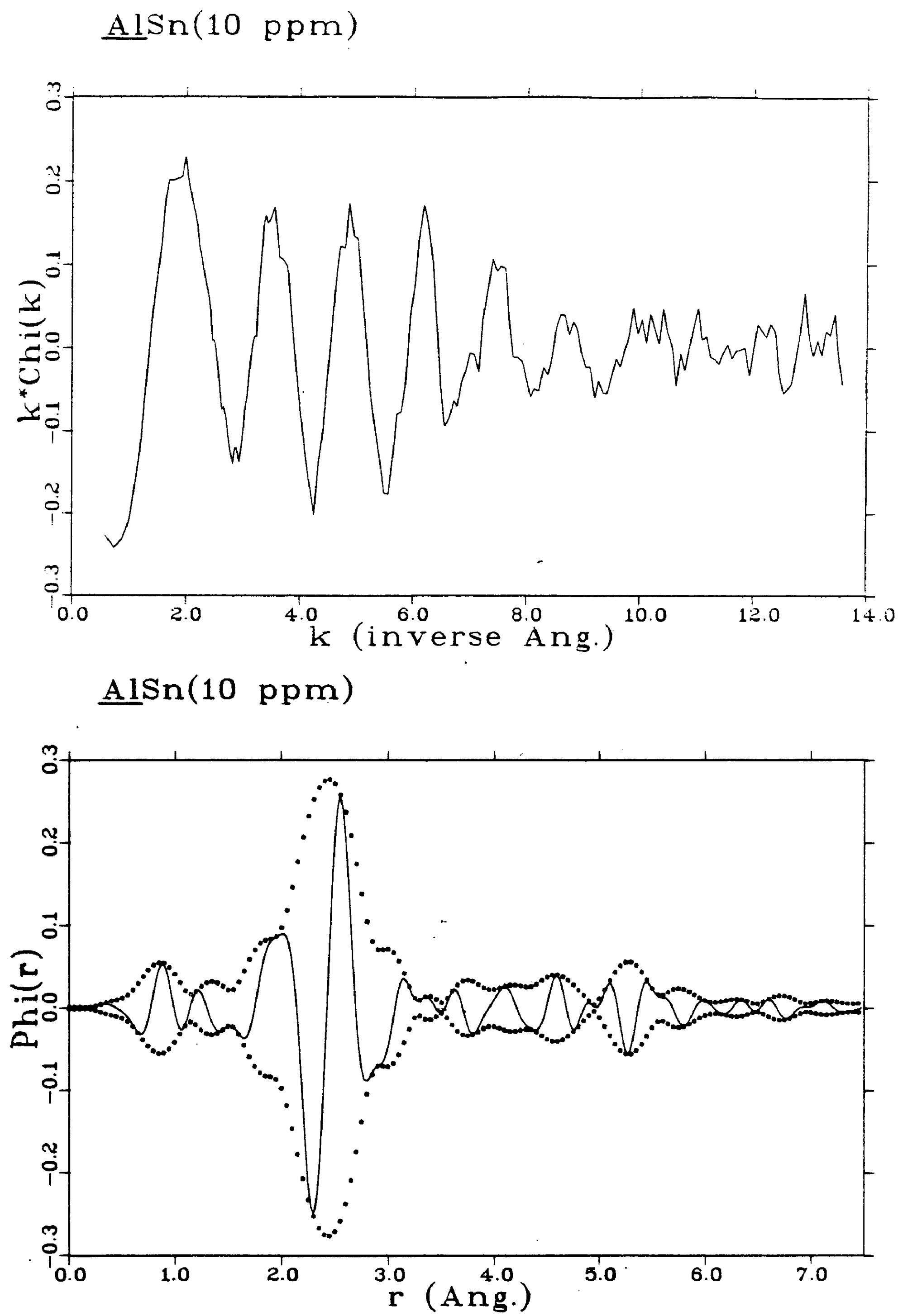

Figure 6.5 $k\chi(k)$ and $\varphi(r)$ for <u>Al</u>Sn(10 ppm) from December 1987. Transform limits: 2.5 to 13.47.

Table 6.2 Fit Parameters for <u>Al</u>Sn(10 ppm).

Signature	No. of Atoms	r, Å	$\Delta\sigma^2$, Å^2	R
Range: 1.90 to 2.95 Å.				
Sn-Al	9.1	2.96	0.004	0.031
Sn-Al	6.7	2.94	0.002	
Sn-Al	2.3	3.04	0.0001	0.030
Sn-Al	7.4	2.94	0.002	
Sn-Sn	0.8	3.00	0.002	0.030
Range: 1.90 to 3.15 Å.				
Sn-Al	11.0	2.98	0.006	0.043
Sn-Al	8.6	2.98	0.002	
Sn-Al	3.6	3.14	0.006	0.037
Sn-Al	7.7	2.95	0.002	
Sn-Sn	3.4	3.06	0.021	0.032
Sn-Al	8.2	2.96	0.003	
β-Sn	0.2*	0.07*	0.006	0.030
<u>Al</u>Sn(50 ppm)	0.77*	0.007*	0.001	0.028

are able to match the sample spectrum to a great degree of accuracy. These fits do show, however, that there is evidence for Sn precipitation in this sample because the R value improved between the two Al peak fit and the one Al peak and one Sn peak fit. The nn number obtained for this range is between 11 and 12 which is more reasonable for an fcc lattice. Although the R values for this fit range are on the order of those obtained for the smaller fit range, this is actually a better fit. Over the larger range, the number of points is greater and the fitting is more constrained, leading normally to a larger residual error R.

When the 10 ppm and the 50 ppm data were fit to each other, a value of R = 0.028 was obtained. This is the lowest R value obtained for the 10 ppm sample but suggests a coordination of only 9 nn. Adding an Al peak or an Sn peak to this fit or considering combinations of 3 Al and Sn peaks leads to unphysical results. Since 9 is an unlikely coordination number for an Al environment and since none of the fits with 2 peaks yields a very low R value, we conclude that the structure of the 10 ppm sample is more complex than that of the 50 ppm. A possible explanation for this is given below.

In addition, the 10 ppm data contains more noise than the 50 ppm data as can be seen in comparing $k\chi(k)$ in Figures 6.4 and 6.5. To get comparable S/N, ~ 5^2 X 7 = 175 10 ppm spectra would have had to have been added together (see Table 5.1). This may be an explanation for the larger R values in the 10 ppm fits.

For the 10 ppm sample, the following has been determined. When the peak itself is fit, the coordination number is found to be ~ 9. Over the larger range, the coordination number is ~ 12, consistent with an fcc lattice. Evidence for Sn precipitation was found in the larger of these ranges. It appears that the Sn environment in the 10 ppm sample is more complex than in the 50 ppm sample. The results of these fits are given in Table 6.2.

Al ion-implanted with Sn. The EXAFS data from this sample are shown in Figure 6.6. Mössbauer spectroscopy measurements of this sample were interpreted as showing that the Sn environment is that of β-Sn [33]. When the data from this sample is fit with the experimental β-Sn spectrum, however, it results in a poor fit (see Table 6.3). In comparing Figures 6.1 and 6.6, it is seen that the peaks in the Fourier transform of the ion-implanted spectrum are narrower than in β-Sn and the relative peak amplitudes are different. Additional fits were also made with β-Sn plus Al and Sn peaks. The fit with β-Sn and one Al peak proved to be nonsensical because it gives a negative amplitude for the Al peak. Fitting the data with β-Sn and one Sn peak decreases the R value to one-half of that obtained for β-Sn.

Fitting with Sn peaks alone, however, proved to be a much more useful approach to determining the structure of this material. Fits were made with Sn peaks at the positions of the first, second, third, and fourth neighbors in β-Sn. The best fit is obtained with Sn peaks at approximately the first through third neighbor positions in β-Sn. (R = 0.019). Including a peak at the fourth neighbor position in the fit

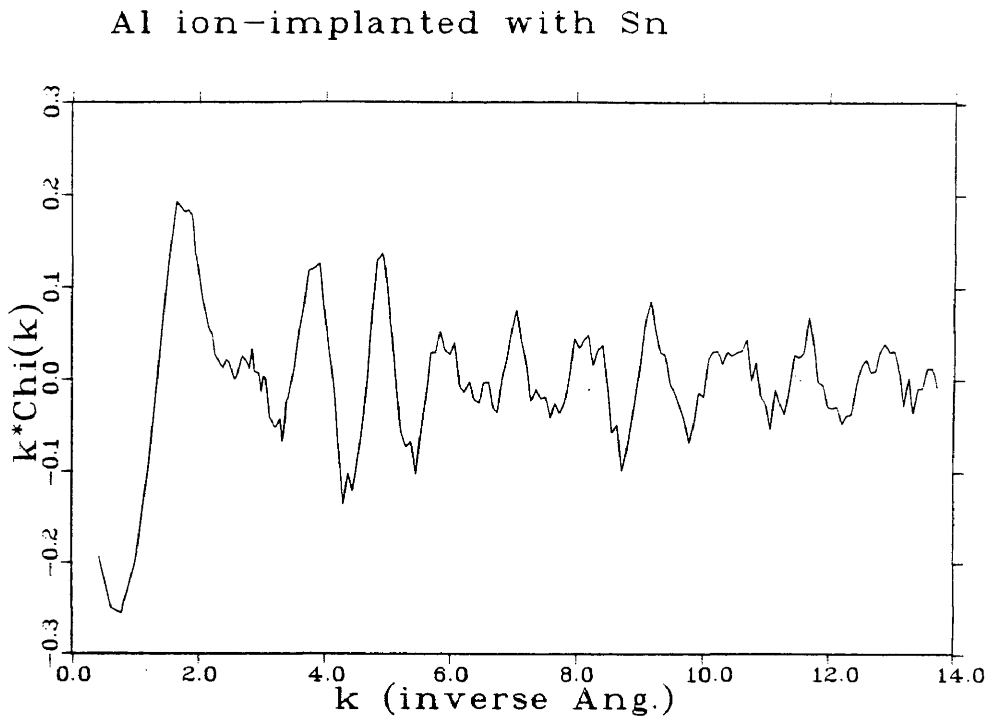

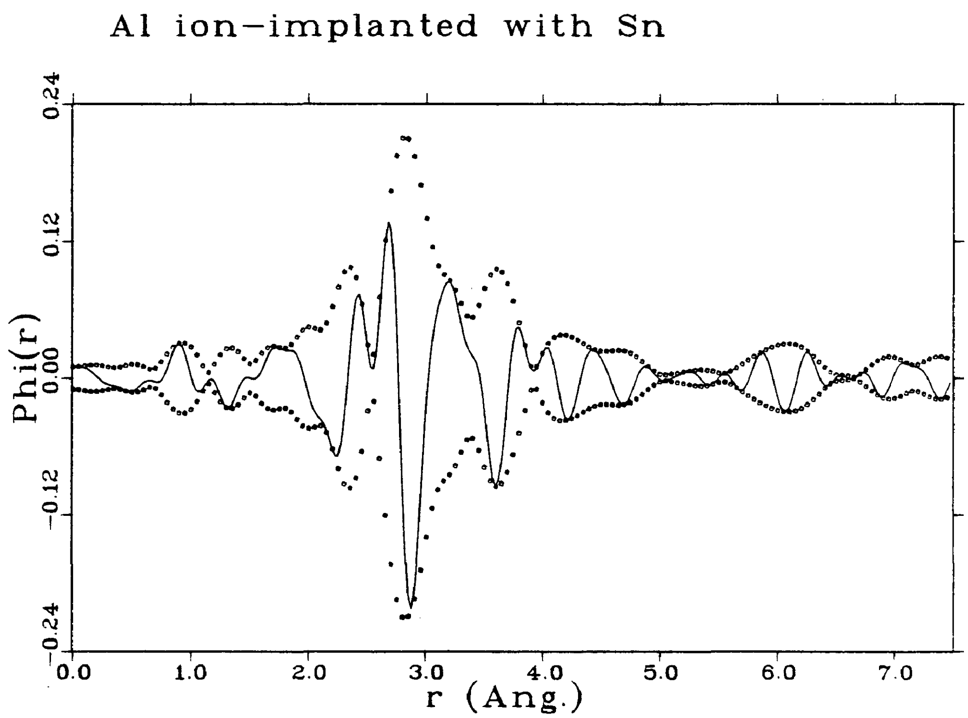

Figure 6.6 $k\chi(k)$ and $\varphi(r)$ for Al ion-implanted with Sn from December 1987. Transform limits: 2.2 to 13.67 $Å^{-1}$.

Table 6.3 Fit Parameters for Al ion-implanted with Sn.

Range: 2.19 to 3.76 Å

Signature	No. of atoms	r, Å	$\Delta\sigma^2$, Å^2	R
β-Sn	0.38*	-0.013*	-0.021	0.051
β-Sn	0.32*	-0.01*	-0.020	
Sn-Sn	0.75	3.03	-0.004	0.024
Sn-Sn	4.6	3.01	0.001	
Sn-Sn	2.0	3.77	0.003	0.023
Sn-Sn	3.3	2.99	-0.002	
Sn-Sn	1.0	3.10	-0.004	
Sn-Sn	2.2	3.78	0.003	0.019

proves not to be useful because it produces an extra peak adjacent to the fit range.

It was suspected that during the process of ion-implantation some α-Sn may have been formed. A fit with β-Sn and a Sn scatterer at the position of the nn in α-Sn, 2.80 Å, was tried. The use of this signature did not, however, improve the R value considerably over β-Sn alone. The results of the fits are summarized in Table 6.3.

For the ion-implanted sample, we find no evidence for Al nn, and therefore conclude that the Sn is predominantly precipitated.

Discussion

We have found that the spectra calculated from the scattering parameters of McKale et al. [29] are accurate in the fitting of EXAFS data. This is supported by the fact that we obtained the number of nn which is expected for an fcc metal and a nn distance which is consistent with other EXAFS studies of dilute alloys. It also indicates that the method of using experimental standards to find corrected scattering parameters and amplitude references is useful.

The most definitive result of this research is the determination of the Sn-Al nn distance in AlSn. This was done using the 50 ppm data for reasons described above. Taking an average of the Sn-Al nn distances found in the fits of the 50 ppm data, this value was determined to be (2.98±0.03) Å. This is remarkably consistent with the sum of the metallic radii of Al and Sn, 2.98 Å [1], as given in Chapter 1. The Al lattice about a Sn impurity is dilated by ~ 0.12 Å, corresponding to an increase of 4 % over the Al-Al nn distance, 2.86 Å. This result is consistent with EXAFS studies of <u>Al</u>Cu [34,35], which also found that the nn distance is approximately equal to the sum of the metallic radii.

A different result was obtained in EXAFS studies of <u>Cu</u>Sn [36] and <u>Ni</u>Sn [37]. The substitutional Sn-host nn distance in these alloys is increased by ~ 0.07 and ~ 0.06 Å, respectively, over the host-host distance. In these alloys, however, the nn distance is found to be ~0.2 Å less than the sum of the metallic radii of the two metals. For Sn in Cu and Ni, there could be hybridization occurring with the host d shells which would cause the nn distance to be less than expected. Al contains no d shells and therefore cannot form hybrids with Sn.

One might expect the structure of the 10 ppm and 50 ppm samples to be nearly identical because the maximum solid solubility of Sn in Al at the annealing temperature (900 K) is ~ 200 ppm. The structure of these samples is different, however, as is discussed above. These differences are proposed to be caused by the following model. As the samples are annealed, an equilibrium concentration of vacancies is formed, calculated by Sørensen and Cotterill to be ~ 100 ppm [12]. When the samples are quenched the vacancies migrate to grain boundaries and free surfaces where relaxation can occur. Since Sn in Al has a positive vacancy binding energy, a certain number of Sn atoms will be dragged along with the vacancies to these areas. In the 10 ppm sample, there is a greater number of vacancies per Sn atom than in the 50 ppm sample. A larger percentage of Sn atoms will then be carried to the grain boundaries than will remain in solid solution. The strain found at grain boundaries leads to much more complex structural possibilities. In addition, there would be a tendency for vacancies which do not relax at the grain boundaries to bind with the Sn atoms, forming Sn-vacancy complexes [12 to 16]. Collisions between Sn-vacancy pairs could also form Sn precipitates [8]. The 50 ppm sample could have a greater fraction of atoms remaining in solid solution than the 10 ppm sample and these atoms would then make the dominant contribution to the EXAFS signal.

The total number of Sn atoms at grain boundaries will also have a large effect upon the structure observed in the EXAFS. An order of magnitude calculation assuming one monolayer of Sn atoms at grain boundaries with an average grain size of one mm shows that at least 10 % of the Sn atoms in the 10 ppm sample could be at grain boundaries, while for the 50 ppm sample it is ~ 1.5 %. In the actual alloy, more than a monolayer can presumably accumulate at the grain boundaries. Assuming 5 monolayers Sn at the grain boundaries, 50 % of the Sn atoms in the 10 ppm sample would be at the grain boundaries and 7.5 % for the 50 ppm sample. This saturation at the grain boundaries would constrain the rest of the Sn atoms in the 50 ppm sample to remain in the grains themselves (~ 90 %).

The Sn environment in the ion-implanted sample was determined to be similar but not identical to that of β-Sn. No Al neighbors were detected. The spectrum is considerably narrower than in β-Sn and the number of scattering atoms appears to be less. The narrowing of the spectrum may lie in the difference between the structures of β-Sn and Al. β-Sn is a much less rigid structure than Al; their Debye temperatures are, respectively, 200 K and 428 K [1]. Conceivably, if small inclusions of β-Sn are introduced into an Al host lattice, they will be influenced by the host lattice and assume a different phonon spectrum. In addition, the process of ion-implantation induces residual stress into the lattice which will tend to make the material much harder. This would be observed in $\varphi(r)$ by a narrowing of the peaks. The fact that the number of scattering atoms appears to be less may be due to an electron mean-free-path effect or many-electron excitations. The process of ion-implantation introduces vacancies and dislocations into the host lattice, many of which do not anneal out. These structural defects tend to decrease the electron mean-free-path. The reduction of the mean-free-path would show up as a reduction in the amplitude of the more distant neighbors, which is what is seen.

It is not surprising that the Sn environment in the sample is found to be similar to β-Sn. If one assumes a dilute distribution of Sn atoms and uses the TRIM89 program [38] to calculate the width of the implanted Sn distribution, one finds that the implanted region is 100 % Sn. While this violates the assumption behind the calculation, one is nonetheless led to conclude that there should be substantial Sn clustering.

This is supported by ion-channeling investigations of Sn ion-implanted Al (doses 1×10^{13} to 1×10^{14} ions/cm^2) by Yagi et al. [39]. They found that even at these low doses most of the Sn was found in precipitates and that as the ion dose is increased this percentage increased. Since the ion dose in the sample analyzed here is ~ 4 orders of magnitude larger than that analyzed by Yagi et al., we might expect the signal detected to be close to that of bulk β-Sn. In order to study dilute Sn ion-implanted in Al, a sample with an ion dose of < 10^{13} ions/cm^2 would have to be analyzed.

Conclusions

EXAFS studies were performed on <u>Al</u>Sn alloys: 50 ppm Sn, 10 ppm Sn, and Sn-ion-implanted Al (dose 5×10^{17} ions/cm^2). This is the first time that EXAFS measurements have been made on such dilute alloys (<100 ppm). The data were fit with calculated scattering parameters published by McKale et al. [29]. To provide an amplitude reference and find corrections to the Sn and Al scattering parameters, Al metal and β-Sn were fit and the results used to generate a calculated Sn-Al spectrum.

The local environment of dilute Sn in Al was found to contain 12 nn including Al atoms at a distance of (2.98 ± 0.03) Å. Remarkably, this value is equal to the sum of the metallic radii of Al and Sn. This is an increase of ~ 0.12 Å over the nn distance in Al and is consistent with EXAFS studies of dilute Cu in Al [34,35].

The structure of the 50 ppm sample is determined to be Sn in solution with some Sn clustering. The structure of the 10 ppm sample is sufficiently complex that the spectrum could not be fit easily. Nonetheless, we find evidence for both Al and Sn nn in the Sn environment in that sample. The Sn-Sn separations in both samples are consistent with the β-Sn structure. Possible Sn environments in these alloys include Sn in solution, Sn clustering and Sn-vacancy complexes. The complex structure of the 10 ppm sample could be caused by grain boundary segregation and vacancy binding of a large proportion of the Sn atoms in the material upon quenching. The 10 ppm sample has a larger number of vacancies and more grain boundary area per Sn atom than the 50 ppm sample.

The ion-implanted sample was determined to resemble β-Sn. The difference between this sample and β-Sn possibly arises from the ion-implantation process.

REFERENCES CITED

1. C. Kittel Introduction to Solid State Physics, 6th ed. New York: Wiley, 1976.

2. N. W. Ashcroft and N. D. Mermin Solid State Physics. Philadelphia: Saunders College, 1976.

3. R. C. Dorward Metallurgical Transactions A 1976, 7A, 308-310.

4. L. F. Mondolfo Aluminum Alloys: Structure and Properties. Boston: Butterworths, 377-380, 1976.

5. K. T. Aust, R. E. Hanneman, P. Niessen and J. H. Westbrook Acta Metallurgica 1968, 16, 291-302.

6. R. L. Eadie and K. T. Aust Scripta Metallurgica 1970, 4, 641-645.

7. Reference 3 from Reference 6.

8. U. Erb and K. T. Aust Scripta Metallurgica 1984, 18, 1263-1265.

9. U. Erb and K. T. Aust Journal of Materials Science Letters 1984, 3, 585-587.

10. K. Iwasaki Phys. Stat. Sol. (a) 1987, 100, 453-459.

11. W. J. Boettinger, P. W. Voorhees, K. C. Dobbyn, and H. E. Burdette Metallurgical Transactions A 1987, 18A, 487-490.

12. K. O. Sørensen and R. M. J. Cotterill Acta Metallurgica 1974, 22, 1331-1338.

13. M. Kato, Y. Ishida, K. Sassa, S. Umeyama and M. Mori Journal de Physique Colloque 1974, C6, 309-313.

14. N. N. Delyagin Soviet Physics - Solid State 1967, 8, 2748-2749.

15. F. T. Pedersen, H. Grann, and G. Weyer Hyperfine Interactions 1986, 29, 1241-1244.

16. C. Szeles, K. Suvegh, Z. Homonnay, and A. Vertes Phys. Stat. Sol. (a) 1987, 103, 397-401.

17. T. M. Hayes and J. B. Boyce, Solid State Physics 1982, 37, 173-351.

18. P. A. Lee, P. H. Citrin, P. Eisenberger and B. M. Kincaid, Reviews of Modern Physics 1981, 53, 769-806.

19. F. G. Bridges, private communication.

20. W. J. Price Nuclear Radiation Detection New York: McGraw-Hill, 1958.

21. A. Guinnier and G. Fournet Small Angle Scattering of X rays New York: John Wiley, 1955.

22. Manual for operational amplifiers AD310J/K and AD311J/K Analog Devices, P.O. Box 280, Norwood, MA 02062 USA.

23. B. Teo, P. A. Lee, A. L. Simons, P. Eisenberger, and B. M. Kincaid Journal of the American Chemical Society 1977, 99, 3854-3856.

24. B. Teo, P. A. Lee, and A. L. Simons Journal of the American Chemical Society 1977, 99, 3856-3859.

25. B. Teo and P. A. Lee Journal of the American Chemical Society 1977, 101, 2815-2832.

26. A. G. McKale, G. S. Knapp, and S.-K. Chan Physical Review B 1986, 33, 841-846.

27. A. G. McKale, S.-K. Chan, B. W. Veal, A. P. Paulikas and G. S. Knapp Journal de Physique Colloque 1986, C8, 55-62.

28. G. S. Knapp, A. G. McKale, S.-K. Chan and B. W. Veal SPIE 1986, 690, 3-8.

29. A. G. McKale, B. W. Veal, A. P. Paulikas, S.-K. Chan, and G. S. Knapp Journal of the American Chemical Society 1988, 110, 3763-3768.

30. G. P. Tiwari and B. D. Sharma Indian Journal of Technology 1973, 11, 557-560.

31. P. Lagarde, private communication.

32. A. Fontaine, P. Lagarde, D. Raoux and J. M. Esteva Journal of Physics F: Metal Physics 1979, 9, 2143-2153.

33. D. L. Williamson, private communication.

34. B. Lengeler and P. Eisenberger Physical Review B 1980, 21, 4507-4520

35. A. Fontaine, P. Lagarde, A. Naudon, D. Raoux, and D. Spanjaard Philosophical Magazine B 1979, 40, 13-30.

36. R. L. Cohen, L. C. Feldman, K. W. West, and B. M. Kincaid Physical Review Letters 1982, 49, 1416-1419.

37. T. J. van Netten, K. Stapel, and L. Niesen Journal de Physique Colloque 1986, C8, 1049-1052.

38. J. F. Ziegler, J. P. Biersack, and U. Littmark The Stopping Range of Ions in Solids, Vol. 1 New York: Pergamon Press, 1985, 232-255.

39. E. Yagi, F. Kano, S. Nakamura, M. Iwaki, and T. Osaka Materials Science Forum 1987, 15-18, 605-610.

Appendix
EXAFS COMPUTER PROGRAMS

In order to analyze the data in this thesis, several computer programs needed to be written and several others were revised from programs written by Dr. Timothy M. Hayes. These programs were all written in FORTRAN 77 for use on the Gould 9750A computer at CSM. The listing of each of the programs is too voluminous to include here, and so the following summary of each of these programs is now given.

The files containing EXAFS data are stored in the binary form in order to conserve computer memory. The extension on each file denotes the type of data file as follows:

.s - indicates data stored as beam intensity (initial, transmitted, fluorescence) vs. monochromator steps.

.e - indicates data stored as x-ray absorption vs. energy.

.k or .l - indicates data stored as $k\chi(k)$ vs. k.

.r - indicates Fourier transform of $k\chi(k)$ (φ) vs. r.

.b - indicates back transform of .r file.

The programs which generate or process these files are discussed below.

The following programs are listed in the order that they would be used in EXAFS data analysis.

a2b - This program converts the ASCII data files generated by the computer at SSRL to a .s file with an appropriate change of header information and data file name.

econ - This program reads a .s file and then converts monochromator steps to energy and takes the appropriate intensities ratio to give the x-ray absorption; For transmission, $\ln(I_o/I_t)$ and for fluorescence, I_f/I_o. Output is a .e file.

cpfit or cpstep - These programs extract $\chi(k)$ from a .e file by two different methods and output, respectively, .k or .l files. cpfit is used for transmission spectra, while cpstep is used for fluorescence spectra. The method used for each is discussed in Chapter 5, pages 51-52.

fft - This program performs a fast Fourier transform upon a .k or .l file with the ability to shift E_0 as needed. Output is a .r file. It will also back transform a .r file with .b as the output.

rsfit - This program performs a fit between the Fourier transforms of a reference file and up to four signature files. This is done by shifting the signatures in r and by varying the magnitude and width of their scattering amplitudes.

The following programs were written to support the above programs in data analysis.

hpplot - a plotting program to plot data on the HP terminal.

sadd - a program to add together sets of steps files (process described in Chapter 5, page 50).

cwf - a program to generate theoretical spectra using the parameters given by McKale, et al. (29).